Correspondence to:

T. W. Becker,
twb@ig.utexas.edu

Generation of Evolving Plate Boundaries and Toroidal Flow From Visco-Plastic Damage-Rheology Mantle Convection and Continents

Thorsten W. Becker[1,2,3] ⓘ **and Lukas Fuchs**[4] ⓘ

[1]Institute for Geophysics, Jackson School of Geosciences, The University of Texas at Austin, Austin, TX, USA, [2]Department of Earth and Planetary Sciences, Jackson School of Geosciences, The University of Texas at Austin, Austin, TX, USA, [3]Oden Institute for Computational Engineering & Sciences, The University of Texas at Austin, Austin, TX, USA, [4]Institute for Geosciences, Goethe University, Frankfurt, Germany

Abstract Earth's style of planetary heat transport is characterized by plate tectonics which requires rock strength to be reduced plastically in order to break an otherwise stagnant lithospheric lid, and for rocks to have a memory of past deformation to account for strain localization and the hysteresis implied by geological sutures. Here, we explore ~10^7 Rayleigh number, visco-plastic, 3-D global mantle convection with damage. We show that oceanic lithosphere-only models generate strong toroidal-poloidal power ratios and features such as a mix of long-wavelength tectonic motions and smaller-scale, back-arc tectonics driven by downwellings. Undulating divergent plate boundaries can evolve to form overlapping spreading centers and microplates, promoted and perhaps stabilized by the effects of damage with long memory. The inclusion of continental rafts enhances heat flux variability and toroidal flow, including net rotation of the lithosphere, to a level seen in plate reconstructions for the Cenozoic. Both the super-continental cycle and local rheological descriptions affect heat transport and tectonic deformation across a range of scales, and we showcase both general tectonic dynamics and regionally applied continental breakup scenarios. Our work points toward avenues for renewed analysis of the typical, mean behavior as well as the evolution of fluctuations in geological and model plate boundary evolution scenarios.

1. Introduction

Earth's lithospheric plates are part of mantle convection, but there is still significant uncertainty as to the appropriate material behavior laws that may capture the evolution of plates. Figuring out which processes control how tectonics is expressed on Earth has implications from the dynamics of fault zone seismicity to constraining long-term planetary evolution.

We know that some frictional or plastic weakening is required to limit the extremely high strengths that purely temperature-dependent viscosity would imply for the lithosphere, or else our planet would be in a stagnant lid (Moresi & Solomatov, 1998; Tackley, 2000a). Focusing on a viscous, long-term fluid flow perspective, models that apply visco-plastic descriptions of rheology in global, spherical convection are, in fact, able to produce many of the hallmarks of plate tectonics (Foley & Becker, 2009; Langemeyer et al., 2021; Mallard et al., 2016; van Heck & Tackley, 2008). However, increasing the yield strength, the transition between mobile, possibly episodic, and then eventually stagnant states is found at yield stresses that appear too low compared to what might be expected from rock mechanics, indicating some additional weakening mechanism(s) such as elevated fluid pressures.

Moreover, specific tectonic features of Earth such as spreading center-transform fault offsets and high degrees of toroidal flow have been suggested to require not just purely plastic behavior but strain localization, that is, a reduction of flow stresses for progressive deformation (Bercovici, 1995b; Bercovici & Ricard, 2013; Gerya, 2010). Such rheological behavior implies a "memory" of prior deformation and hysteresis can arise in a number of different ways. Geologically and from plate reconstructions, there is evidence that existing zones of lithospheric weakness can in fact be reused after perhaps as long as a billion years (e.g., Buiter & Torsvik, 2014; Burke et al., 1977).

A range of microphysical mechanisms have been debated (Montési, 2013), but one candidate for a localizing rheology with memory is grain size evolution within dislocation-diffusion creep (e.g., Bercovici & Ricard, 2013; Landuyt et al., 2008). An approximation to such behavior is provided by tracking the effects of a quasi-strain,

damage variable that reduces yield strength (e.g., Lavier et al., 2000; Ogawa, 2003; Tackley, 2000a) and can heal through thermal processes. For appropriate parameter choices, such a description can capture aspects of more complex grain-size evolution laws (Fuchs & Becker, 2021) and allows for a relatively simple exploration of what may approximate bulk memory-controlled behavior. We have recently explored the dynamics of global, 3-D, visco-plastic convection models with this rheology using relatively low, $\sim 10^6$, Rayleigh number computations for an idealized, oceanic lithosphere-only planet and found that reactivation of self-consistently formed, persistent weak zones led to more rapid reorganizations of tectonics and heat transport (Fuchs & Becker, 2022).

Here, we explore models with ~ 10 times higher convective vigor which appear nearly Earth-like in terms of their convective planform, internal structure, as well as surface kinematic power spectra. By comparison with kinematic constraints from plate reconstructions, we can explore potential avenues for narrowing down appropriate rheological laws to capture and then later predict plate boundary evolution. Earth's mantle is not purely in a thermal convection state, of course, and the thermo-chemical component as expressed by continental crust and lithosphere at the surface is here additionally explored as a major complication in such analysis.

2. Observational Constraints and Modeling

2.1. Plate Tectonic Models and Plate Kinematics

We proceed to analyze a range of plate models and reconstructions in terms of their kinematic power spectra. Such an analysis has a long history (Čadek & Ricard, 1992; Lithgow-Bertelloni et al., 1993; O'Connell et al., 1991), but modern plate models have not been evaluated comprehensively in this fashion, to our knowledge. More importantly, it is useful to consider the range of these metrics for plate geometries and plate speeds, or, equivalently, the degree of intraplate deformation. All of those properties can be summarized in this way in a statistical sense which lends itself for comparison with general convection models, as opposed to those tailored for a specific region or time period of Earth's lithosphere. There are a number of other ways of evaluating the typical character of plate tectonic reconstructions but here we focus on the kinematics and explore the general behavior of our global damage convection models.

One way to analyze horizontal velocity fields, $\hat{\boldsymbol{u}} = \{0, u_\phi, u_\theta\}$, is by Helmholtz decomposition into poloidal (source/sink, vorticity free), $\boldsymbol{u}_p$, and toroidal (vorticity generated, source-free) velocity, $\boldsymbol{u}_t$, components

$$\boldsymbol{u}_p = \hat{\nabla} V \quad \text{and} \quad \boldsymbol{u}_t = -\boldsymbol{e}_r \times \hat{\nabla} W, \tag{1}$$

where V and W are the scalar poloidal and toroidal potentials, respectively, $\boldsymbol{e}_r$ a unity radial vector, and $\hat{\nabla}$ the horizontal gradient operator. For global, spherical $\hat{\boldsymbol{u}}$, the potentials V and W can be computed by expansion into vector spherical harmonics (e.g., O'Connell et al., 1991). The horizontal divergence, $\hat{\nabla} \cdot \boldsymbol{u}$, and vertical component of the vorticity, $(\nabla \times \boldsymbol{u})_r$, relate to the potentials via Laplacian equations, $\hat{\nabla}^2 V = \hat{\nabla} \cdot \boldsymbol{u}$ and $\hat{\nabla}^2 W = (\nabla \times \boldsymbol{u})_r$ and can be recovered from the spherical harmonic coefficients of V and W. Features on spatial scales of D relate to spherical harmonic degree ℓ as $D \sim 20,000 \text{ km}/\ell$, and we carry all expansions up to $L = \max(\ell) = 255$.

Figure 1a shows the power (summed, squared coefficients per degree and unit area) spectrum, $\sigma(\ell)$, for both poloidal and toroidal coefficients for the current plate motion model MORVEL (Argus et al., 2011) which has plate geometries from Bird (2003). As discussed by O'Connell et al. (1991), the poloidal and toroidal power spectral decay as in Figure 1a reflects the discontinuous nature of velocity amplitudes as per the rules of plate tectonics, that is, no deformation within plates. The spectral decay seen in the plate kinematics is thus roughly that of a step function; this is illustrated by comparison with the power spectrum of a scalar function where unity is assigned to regions within the Pacific plate and zero else (gray line in Figure 1). The decay of σ is well captured at high ℓ with a power-law with $\sigma \sim \ell^\beta$ and $\beta \gtrsim -3$, where -3 is the theoretical Heaviside expectation, and $\beta \approx -2.9$ for MORVEL (Figure 1a).

When averaged over ℓ, the ratio of toroidal to poloidal power, TPR, is $\approx 55\%$ across a wide range of degrees for current plate motions, with the $\ell = 2 \dots 20$ ratio being 57% (Figure 1a). This is one of the hallmarks of the Earth's style of modern tectonic heat transport, and an important metric to consider when evaluating convective models of plate generation. The reason for this relatively high-power stirring motion is not immediately obvious since only poloidal flow is associated with vertical transport of mass and hence convective cooling. We know that lateral viscosity variations are required to excite toroidal flow across all degrees (O'Connell et al., 1991; Ricard
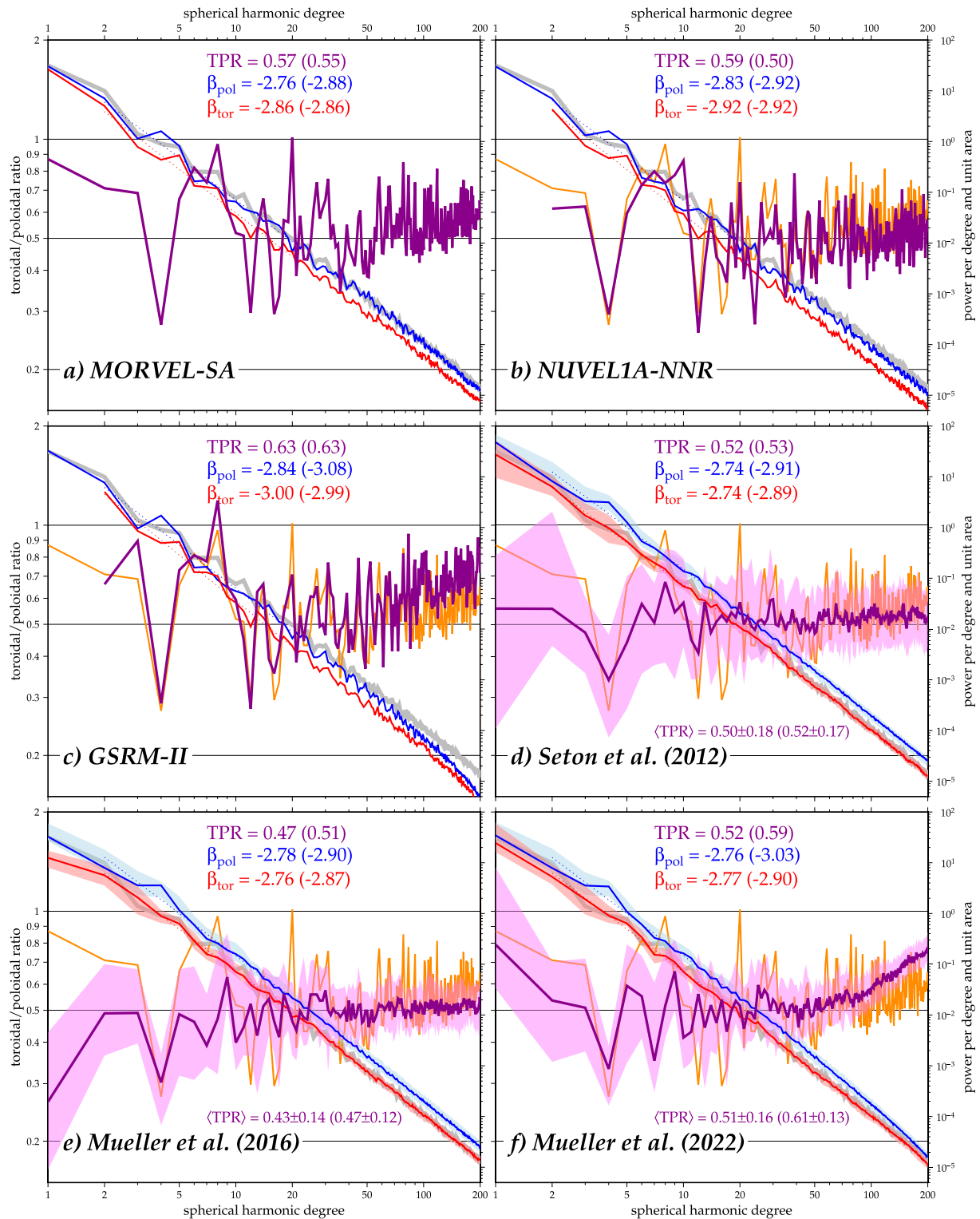
Figure 1. Poloidal (σ_P, blue) and toroidal (σ_T, red) velocity power and their ratio (TPR, magenta), for present-day (a–c) and time-evolving (d–f) plate kinematic models. For plate tectonic reconstructions, we show the temporal median and in light shading the 25/75% quartiles, going back to 140 Ma only to focus on relatively well-constrained time periods (cf. Torsvik et al., 2008). Legend states best-fit power-law exponents, for example, $\sigma_P \propto \ell^{\beta}$, and median TPR over $1 \leq \ell \leq L$ for $L = 20$, and $L = 200$ for the values in parentheses, as applied to the temporal median spectra. $\langle TPR \rangle$ values state the temporal mean and standard deviation over time-dependent average TPR. Orange line in panels (b–f) is the TPR of the MORVEL-SA model in panel (a), and gray line is the power spectrum of an arbitrarily scaled MORVEL Pacific plate-geometry step function, both shown for reference.

et al., 1991). For spherical geometries, toroidal motion may, in fact, serve to lower the overall viscous dissipation within the mantle, making the system work more efficiently (Bercovici, 1995a). However, the excitation of the right kinds of toroidal fields as represented by Figures 1a–1c has been suggested to require strain-localization, for example, damage-dependent rheologies, and purely plastic or power-law behavior alone may be insufficient (Bercovici, 1995b; Bercovici & Ricard, 2013).

Figure 1a shows MORVEL power spectra from expanding velocities in the spreading-aligned absolute plate-motion reference frame (Becker et al., 2015) which has a moderate net rotation (NR), that is, $\ell = 1$ toroidal flow, component for the present-day. This NR power is typical of a range of estimates, for example, from global hotspots (Becker et al., 2015) and works out to TPR($\ell = 1$) $\sim$80%…90%. This rate of NR is comparable to the net rotations excited by sub-continental to sub-oceanic asthenospheric viscosity variations in global mantle circulation models with present-day continent or cratonic geometries (Becker, 2006; Ricard et al., 1991; Zhong, 2001).

Any plate motion model depends on sometimes subjective choices such as where to impose plate boundaries (e.g., Bird, 2003), and we proceed to compare two rigid plate descriptions of crustal motions, and one explicitly allowing for intraplate deformation. Figures 1b and 1c show the power spectra of different representations of present-day crustal motions, both in a no-net-rotation reference frame. Figure 1b shows results from the NUVEL model (DeMets et al., 1990), which has fewer plates than MORVEL, and illustrates the effects of such differences on β and the median TPR. Degrees 2…10 are very similar between MORVEL and NUVEL since they are controlled by the large plates' geometry. The median NUVEL TPR for $\ell = 2…20$ is slightly larger than for MORVEL, $\approx$60%. Figure 1c is based on the deforming plate, GSRM model in the version of Kreemer et al. (2014) which includes information from geodesy. Allowing for such a, presumably more realistic, representation of lithospheric deformation leads to a more rapid decrease in poloidal power at high degrees, and consequentially, an increase of the TPR for $\ell \gtrsim 50$ from the $\sim$60% plateau for $2 \leq \ell \lesssim 20$, compared to the MORVEL or NUVEL representations. The $\ell \leq 20$ TPR of this deforming plate model is also increased, to 63%.

While present-day plate models are providing the most detailed information on lithospheric deformation, plate motion reconstructions can provide some insights into the typical fluctuations of parameters. Broadly speaking, the TPR of the median power spectra is close to $\approx$50% over all degrees for the last 140 Ma (Figures 1d–1f). This is slightly reduced but comparable to the present-day values, substantiating the analysis based on earlier plate reconstructions (Čadek & Ricard, 1992; Lithgow-Bertelloni et al., 1993). Much of the present-day structure of the TPR as a function of degree gets averaged out by the evolution of the plate system, with the exception of $2 \leq \ell \lesssim 6$ patterns associated with the dominance of the circum-Pacific subduction system. The decay of both the temporal median poloidal and toroidal power is with $\beta = -2.7…-2.8$ on average for $2 \leq \ell \leq 20$, as for the present-day. The rigid plate reconstructions by Seton et al. (2012) and Müller et al. (2016) are typical in terms of their β values, and the variations over time as indicated, for example, in the range of TPR fluctuations throughout the Cenozoic. There is thus significant variability in the average TPR across degrees over time, with a standard deviation of 0.14…0.18 for $\langle TPR \rangle$, meaning that toroidal power typically fluctuates between $\sim$30% and 70%. Time-averaged mean TPR values are close to the TPR of the median power spectra, with 0.43 $\pm$ 0.14 for Müller et al. (2016) on the lower end (Figure 1e).

Temporal fluctuations in the power spectra are particularly large for the $\ell = 1$, NR terms (Rudolph & Zhong, 2014) and the geophysical and geological constraints are compatible with a range of NR values (Tetley et al., 2019). However, time-evolving convection models indicate that moderate values, for example, of Figure 1a with TPR($\ell = 1$) $\lesssim$ 80%, might be typical (Atkins & Coltice, 2021). The time-averaged TPR($\ell = 1$) from Seton et al. (2012) and Müller et al. (2016) are $\approx$56% and $\approx$26%, respectively, from the median spectra of the last 140 Ma. Plate tectonic reconstructions can also allow for deforming plate interiors and the model by Müller et al. (2022) is shown as an example in Figure 1f. As for the GSRM model of Figure 1c, the TPR consequentially is higher for $\ell \gtrsim 50$ than for the rigid plate models because poloidal power decays more rapidly with ℓ than the toroidal contributions. Realizing the range of uncertainties associated with plate reconstructions even for the last 140 Ma (e.g., Torsvik et al., 2008), and recognizing some of the inter-model differences, we choose the median TPR of Müller et al. (2016) as in Figure 1e as a reference for our plots, but will also compare to the deforming plate approaches.

2.2. Observational Constraints on Deep Structure

For the present-day mantle, we can also rely on structural seismology, for example, as expressed as the power spectrum of shear wave velocities. While there are complexities due to composition and mineral physics, as well as tomographic smoothing, such heterogeneity spectra provide information on the nature of convection (Bunge et al., 1997; Tackley et al., 1994). Figure 2a shows the depth-dependent spectrum of the shear wave model TX2019 (Lu et al., 2019) which includes a priori information on Wadati-Benioff zones. As is typically found, $\ell = 2$ structure is dominant throughout much of the mantle, and the thermo-chemical surface boundary layer of the lithosphere ≲300 km contains much of the overall heterogeneity. As can be seen from the depth-dependent spectral moment curve (cyan line in Figure 2a), the power distribution shows the shortest wavelength moment below the lithosphere, with a more subtle higher ℓ bump at ~700 km (Boschi & Becker, 2011), likely associated with viscosity and phase changes (Bunge et al., 1997; Tackley et al., 1994). There is another subtle transient toward increased higher ℓ heterogeneity with depth at ~2,000 km which may be associated with compositional heterogeneity increasingly below those depths, for example, due to thermo-chemical piles or drags closer to the core-mantle boundary (Deschamps & Tackley, 2009).

While there is still some debate as to the links of seismological power spectra with mantle convection, it is clear that the length-scales associated with plate-tectonic style motions serve to organize convection toward lower-ℓ, redder spectra compared to free, isoviscous convection (Buffett et al., 1994; Zhong et al., 2000). Previous visco-plastic, plate-like thermal convection models produced power-spectra similar to those inferred from tomography (Foley & Becker, 2009; Mallard et al., 2016). While $\ell = 1$ dominance appears more typical (Yoshida, 2008), some choices of plasticity values do yield $\ell = 2$ dominated structure in purely oceanic lithosphere models (Foley & Becker, 2009). We do, however, expect more realistic models with continents to show more pronounced $\ell = 2$ patterns, as well as cyclic variations from hemispheric, $\ell = 1$, to Pacific, Ring-of-Fire type $\ell = 2$ scenarios (Coltice et al., 2012; Zhong et al., 2007).

2.3. Theoretical Approach and Numerical Methods

We approximate mantle convection by the equations governing laminar fluid flow in the incompressible, infinite Prandtl number regime. In this case, conservation of mass, momentum, and energy can be written as

$$\nabla \cdot \boldsymbol{u} = 0 \tag{2}$$

$$-\nabla p + \nabla \cdot (\eta \dot{\epsilon}) = (Ra\,T + Rb\,C)\boldsymbol{e}_r \tag{3}$$

$$\frac{\partial T}{\partial t} + (\boldsymbol{u} \cdot \nabla)T = \nabla^2 T + H, \tag{4}$$

where all variables are in non-dimensionalized form as in McNamara and Zhong (2004). Here, $\boldsymbol{u}$ is velocity, p dynamic pressure, η viscosity, $\dot{\epsilon}$ the strain-rate tensor, Ra and Rb the thermal and compositional Rayleigh numbers, respectively, T and C non-dimensional temperature and composition, respectively, and H internal heat production. All computations have Ra = 10^8 when based on radius (McNamara & Zhong, 2004; Zhong et al., 2000), with convective vigor discussed below.

To solve these equations, we use the finite element code `CitcomS` (Moresi & Solomatov, 1995; Zhong et al., 2000) with the tracer implementation of McNamara and Zhong (2004) which is used to track the nominally diffusion-free and source-less C field according to

$$\frac{\partial C}{\partial t} + (\boldsymbol{u} \cdot \nabla)C = 0, \tag{5}$$

where C denotes continental material with different strength and buoyancy (see below). Our general setup closely follows Fuchs and Becker (2022); we consider purely internally heated convection and use visco-plastic rheologies with damage to explore plate-like planforms of convection.

Our basic choices for rheology are an attempt to make surface motions as plate-like as possible before introducing and exploring the effects of damage. The starting viscosity is depth and temperature-dependent

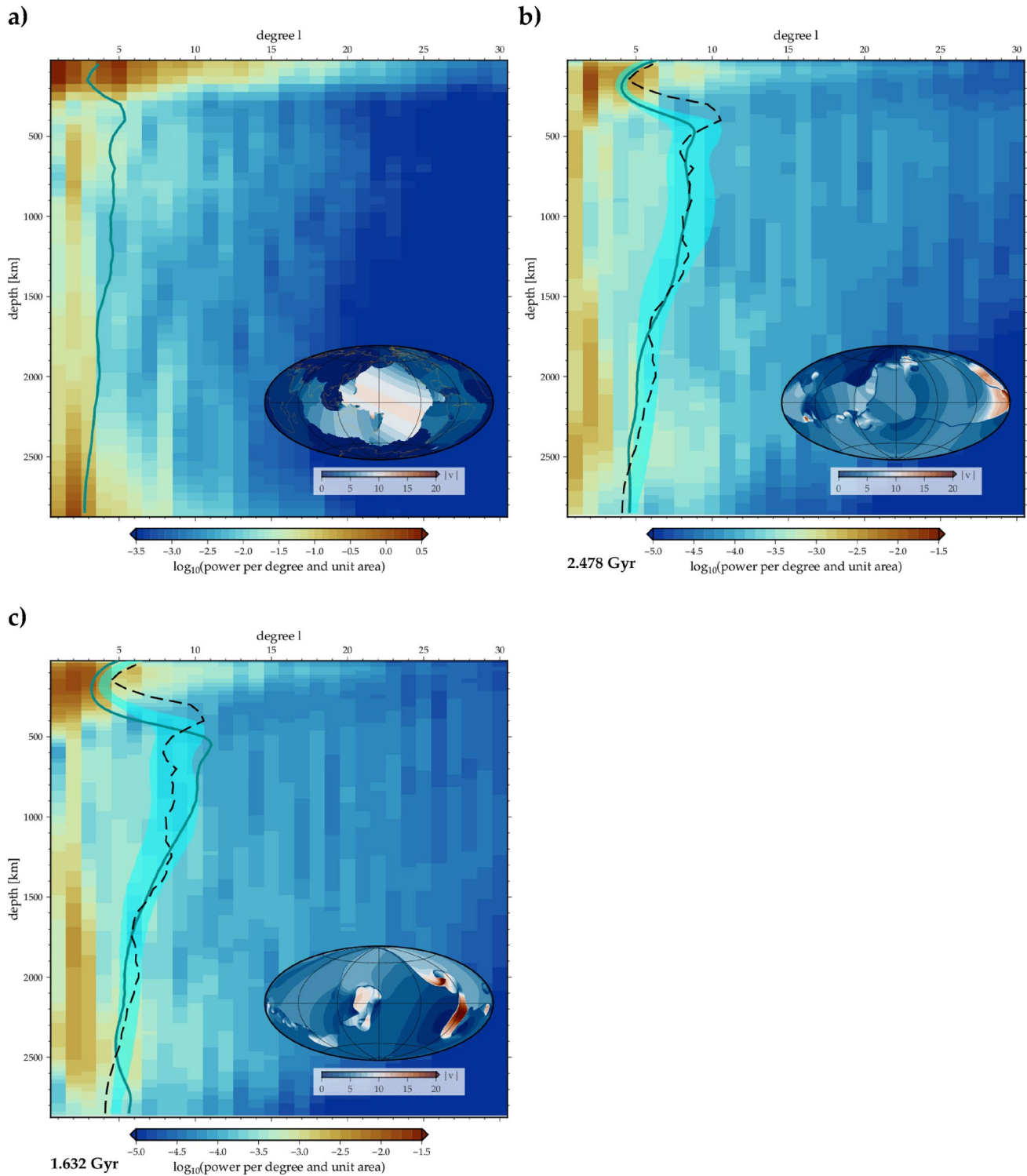$$\eta_T = \eta_0 \exp\left(\frac{E}{T+1} - \frac{E}{2}\right), \tag{6}$$

Figure 2. Power, $\sigma(\ell)$, per degree and unit area on a log-scale (background) as a function of depth and spherical harmonic degree, ℓ, as well as a power-weighted spectral moment curve (cyan) indicating the typical frequency content at each depth. Inset shows surface velocity amplitudes in cm/yr on Hammer projection. (a) σ_{v_S} from the shear wave velocity anomalies of TX2019 (Lu et al., 2019), with surface velocities for MORVEL, as in Figure 1a. (b) σ_T based on a snapshot of a typical 3-D temperature distribution from a damage convection model without continents (model 22 of Table 1). Lightly shaded region indicates 25/75% range around the median spectral moment over time, solid line the current moment. Dashed line is the tomography spectral moment from panel (a), but arbitrarily scaled with $\ell^{1.4}$ to fall within the convection model range. (c) Different snapshot of the same convection model where much of the spectrum with depth is dominated by $\ell = 2$.

Table 1
Parameters for the Main Models Discussed in the Text, All Non-Dimensional

Model Name	Code	Yield stress, a (10^6)	d affects	Crit. str. (d_{cr})	Red. factor (Γ)	Temp.-dep. heal. (E_d)	Heal. rate B (10^9)	Continents
Reference	19	1	σ_y	10	0.9	46.1	2.44	None
Slow heal.	22	1	σ_y	10	0.9	46.1	1	None
Visc. dam.	25	1	η_0	10	0.99	46.1	1	None
High a	25_hy5	1.25	η_0	10	0.99	46.1	1	None
1 cont.	19_1	1	σ_y	10	0.9	46.1	2.44	1
2 cont.	19_2	1	σ_y	10	0.9	46.1	2.44	2
3 cont.	19_3	1	σ_y	10	0.9	46.1	2.44	3
5 cont.	19_5	1	σ_y	10	0.9	46.1	2.44	5
5 cont., High H_c	19_5h	1	σ_y	10	0.9	46.1	2.44	5

Note. All computations have a thermal Rayleigh number of Ra $= 10^8$ based on radius (McNamara & Zhong, 2004), purely internal heating, reference temperature-dependence of viscosity of $E = 40$, and viscosity variations additionally limited to eight orders of magnitude variation from η_0. As in Fuchs and Becker (2022), the reference yield stress, σ_y, varies with non-dimensional depth, z as $\sigma_y = a + bz$, with $a = 10^6$ and $b = 1.51 \cdot 10^7$. Continental rafts are harder to yield at $a_c = 10a$, and compositionally buoyant with $Ra_b = -0.75$ Ra. Internal heating within continents is that of the mantle, $H_c = H = 120$, except for model "high H_c" which has $H_c = 240$ and $H = 115.8$. For $H = 120$, when expressing Ra in terms of mantle thickness, Ra_D, the internal heating Rayleigh number is thus $Ra_D H \sim 1.1 \cdot 10^9$, and when further adjusted for a typical depth-average of viscosity $\langle \eta_0 \rangle \sim 100$ (Figure A1), the effective Rayleigh number is $\sim 10^7$. Parameters are otherwise as in Fuchs and Becker (2022).

where η_0 is a reference viscosity, E controls the strength of temperature dependence. The η_0 parameter is globally reduced by 0.1 within the equivalent of 100…400 km depth to mimic the effects of an effectively depth-dependent asthenospheric weak zone (Figure A1). Additionally, we use a further, "melt" asthenospheric viscosity reduction which mainly occurs underneath young oceanic plates, by multiplying η_0 with an additional factor of 0.1 if $T \geq 0.6 + 2(1 - z)$, where z is depth normalized by layer thickness (Tackley, 2000c). The effects of these choices are discussed in Section 3.1.3.

A further plastic limiter viscosity $\eta_P = \sigma_y/(2\dot{\epsilon}_{II})$ applies, where $\dot{\epsilon}_{II}$ is the second invariant of the strain-rate tensor and σ_y yield stress. The yield stress changes according to $\sigma_y = a + bz$, where z is depth; this ignores any dynamic pressure-dependence of yielding and may underestimate localization in the shallow lithosphere. The total viscosity is given by the minimum, $\eta = \min(\eta_T, \eta_P)$, akin to earlier, quasi-plastic models (Moresi & Solomatov, 1998), and η is further limited to eight orders of magnitude variations to limit huge lithospheric viscosity values. On small spatial scales, ~ 100 km, viscosity typically changes by $\lesssim$four orders of magnitude.

Unlike most previous, global plate-generating convection modeling, with the exception of Fuchs and Becker (2022), we also explore the role of damage rheology for the planform of convection. For this, we use a simplified description that tracks a damage variable d using tracers and integrating over $\dot{\epsilon}_{II}$ and allowing for healing (Ogawa, 2003; Tackley, 2000a)

$$\frac{\mathrm{d}d}{\mathrm{d}t} = \dot{\epsilon}_{II} - d \exp\left(-\left(\frac{E_d}{T+1} - \frac{E_d}{2}\right)\right)B, \qquad (7)$$

where B is the healing rate, and E_d quantifies the temperature-dependence of healing akin to Equation 6, for simplicity. With typical choices, this formulation can lead to the persistence of damaged regions up to $\gtrsim 100$ Myr in the shallow, cold lithosphere (Fuchs & Becker, 2021), which is comparable to overturn times for Earth, and damage can be sustained for typical plate lifetimes in our models (Fuchs & Becker, 2022).

We can then link d to a reduction of the yield stress, σ_y, or the viscosity pre-factor, η_0, for example, using a linear relationship with some constant factor $\Gamma \in [0; 1)$, for example, of order 0.9 (e.g., Lavier et al., 2000)

$$\sigma'_y = \sigma_y \left(1 - \frac{\min(d, d_{cr})}{d_{cr}}\Gamma\right), \qquad (8)$$

and equivalent for η_0. Such strain-dependent weakening and hardening of the plastic or creep part of the viscosity by means of tracking damage d is highly simplified compared to a range of microphysical mechanisms proposed to account for strain localization and persistent sutures in nature. However, which mechanisms may be relevant for nature remains debated, and we view the damage treatment as a useful approximation that may eventually provide constraints for the range of actual micro-physical mechanisms. Moreover, our simplified description can mimic many aspects of grain-size dependent creep (Fuchs & Becker, 2021), which is one of the major candidates for strain-localization and memory within mantle convection (e.g., Bercovici & Ricard, 2013; Landuyt et al., 2008).

Unlike Fuchs and Becker (2022), we use a stronger temperature-dependent viscosity and a ~10 times higher Rayleigh number. Our internal heating Rayleigh number is $\mathrm{Ra}_D H = 1.1 \cdot 10^9$ nominally when computed for mantle thickness (Table 1) but when correcting for the depth-averaged viscosity, the effective, layer-based Rayleigh number perhaps best suited to compare convective vigor is reduced to ~10^7 (Figure A1). Scaled surface heat flux for the models is ~34 TW (Section 3.1.1), close to the ~36 TW for the convective part of Earth at present (Jaupart et al., 2015). However, with the convective vigor for our reference model, our dimensional velocities are ~0.1 of typical present-day plate velocities, perhaps indicating a slight deviation from boundary layer scaling expectations. Choosing surface velocities as a reference, we rescale dimensional times by a corresponding 0.1. We ran ~50 such high Rayleigh number models but only discuss what we consider the most interesting model variations in the main text with parameters for these models listed in Table 1.

In another departure from Fuchs and Becker (2022), we also explore the role of continental rafts (cf. Coltice et al., 2012; Phillips & Bunge, 2005; Rolf et al., 2012; Zhong & Gurnis, 1993). The latter are implemented by tracking a composition C with tracers (McNamara & Zhong, 2004), and seeding with 30 tracers per element. We prescribe $C = 1$ within the top 300 km of the mantle underneath continental regions, and $C = 0$ else in the mantle. Within regions where $C > 0.5$, a 10 times higher yield stress offset applies (Table 1), and compositional buoyancy affects body forces, Equation 3, via $\mathrm{Ra}_b = -0.75\,\mathrm{Ra}$ to approximate an isopycnic, strong continental lithosphere (cf. Jordan, 1978; Lenardic et al., 2003). The same tracers used for tracking C also carry the damage variable d as an additional property, as in Fuchs and Becker (2022).

We ran all models for several convective overturn times before analyzing their character, for example, when computing time-averaged kinematic power spectra. We averaged these metrics for as long as possible to obtain characteristic values. In doing so, we tried to avoid clearly episodic states by visual inspection of surface velocities and heat flux variations, and episodicity was most prevalent for models with continental rafts. However, the strong time dependence of the evolving plate boundary system makes averaging a challenging proposition, and it is difficult to fully avoid transient switches in tectonic states.

Most computations were run at a uniform resolution of ≈26 km horizontally and 22 km vertically. This reference resolution appears sufficient to capture the broad-scale behavior based on comparison with a number of tests run for shorter periods of model time at higher resolution of ≈7 km horizontally and 22 km vertically throughout the mantle with refinement to ≈7 km vertically in the surface boundary layer. While different in detail, broadly the evolutionary character and kinematic metrics of these models were in agreement. This is illustrated by the specific evolutionary scenario of Figures 12 and A4, and a comparison of the general state of the system of Figures A2 and A3. We did find that models that had σ_y affected by d were more stable numerically than those where damage applied to η_0 for higher resolution cases, implying that such viscosity weakening cases may suffer from mesh dependence. While we are confident that our models are overall robust with respect to resolution, other rheological choices may produce qualitatively different results on smaller, plate-boundary scales, but further verification and exploration of such issues are outside our current computational resources.

3. Results

3.1. Overall Character of Models

3.1.1. Surface Kinematics and Heat Transport

Our global convection models show a range of interesting tectonic features, most of which are highly time-dependent. Figure 3 shows a snapshot of the reference model's surface expression of mantle convection, and we also provide movies illustrating the temporal evolution of a few key models in Appendix A. As for earlier visco-plastic models (Foley & Becker, 2009; van Heck & Tackley, 2008), most deformation is found to be
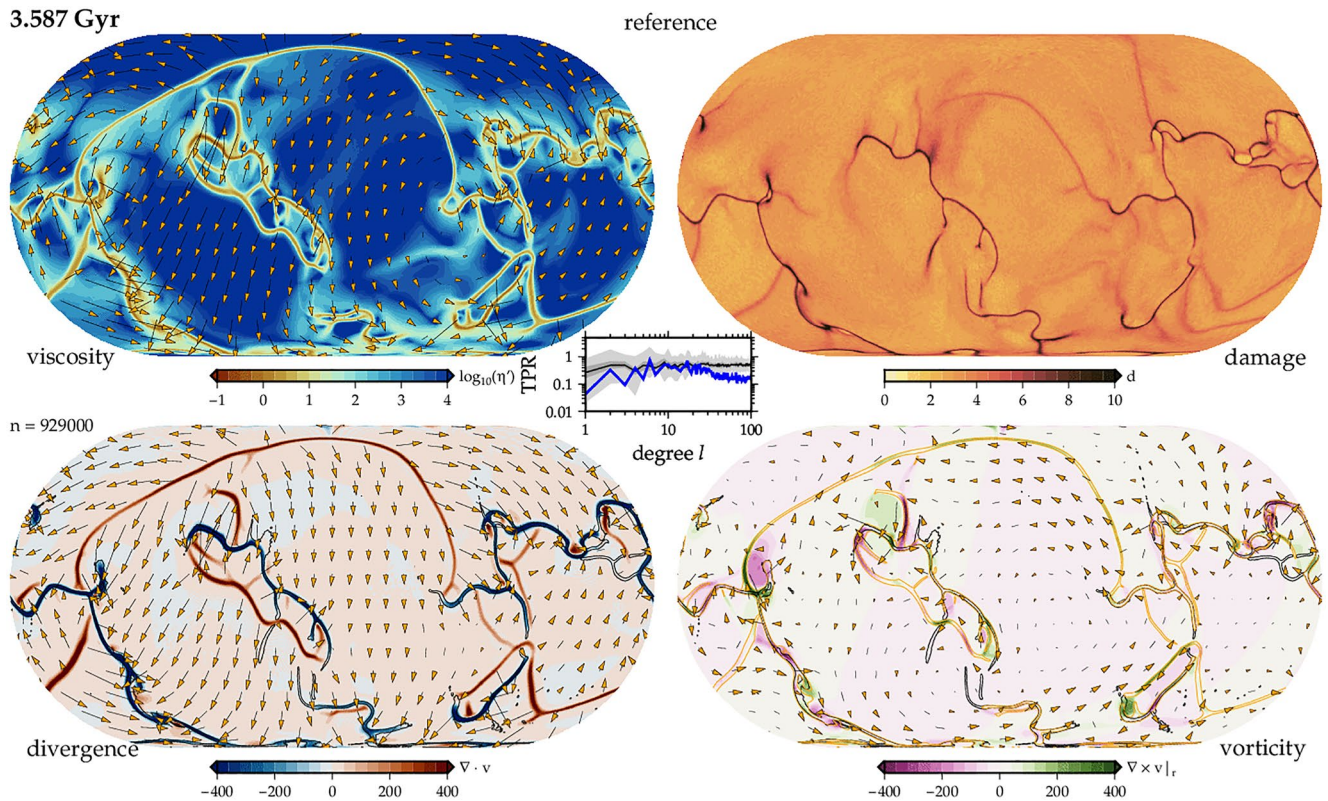
Figure 3. Surface dynamics of the reference model (19 of Table 1) from a snapshot of viscosity (log-scale of normalized viscosity, $\eta' = \eta/\eta_0$) and velocity (orange vectors, top left), damage (top right), poloidal velocities and horizontal divergence (bottom left), and toroidal velocities and vertical vorticity (bottom right; all Eckert-IV projection). Orange and black contours denote active plate boundaries ($\log_{10}(\eta') = -2, -1, 0, 1$) and high damage ($d = 5$) regions. The central plot shows the toroidal:poloidal ratio (TPR) as a function of spherical harmonic degree ℓ in blue, compared to the median and range back to 140 Ma from Müller et al. (2016), as in Figure 1e. Animations of the time-dependence which allows evaluating plate boundary evolution, for example, are provided in Appendix A for all models.

localized in plate boundary zones, making the planform of surface motions appear akin to our present-day style of tectonic motions in this sense.

Overall, the rheological choices work out such that plate interiors are ~5 orders of magnitude higher in viscosity than the interior of the shear zones found within plate boundary zones. Given our choices of rheological parameters, this range of variation is slightly less than in the purely visco-plastic computations of Langemeyer et al. (2021), for example, which is partially because of damage and corresponding sutures (Fuchs & Becker, 2022). There are also some broad, intraplate deformation zones that are ~1,000 lower in viscosity than the interior of the plates. This range of effective viscosity variations is broadly consistent with global constraints on intraplate deformation (Becker, 2006), for example, Our reference numerical resolution appears sufficient to capture the dynamics, though higher resolution models may enhance plateness slightly (cf. Figures A2 and A3).

As for our earlier, lower Rayleigh number models (Fuchs & Becker, 2022), existing weak zones based on persistent damage regions in the lithosphere are affecting local plate dynamics (e.g., movies in Appendix A). Unlike our earlier experiments, we find more of a mix of large plates produced by long-wavelength convection and smaller tectonic features, such as arcuate zones of downwellings with complex spreading center morphology, similar to those documented by Mallard et al. (2016). Zones of plate consumption are overall smaller-scale than the spreading centers (see, e.g., the divergence in Figure 3). This is partly a function of the latter being entirely passive features since we are only considering purely internally heated models (Foley & Becker, 2009; Tackley, 2000b). The mean and standard deviation of the heat flux over time are 33.6 ± 1.7 TW, that is, a ≈5% fluctuation around the mean (Figure 4).

The total toroidal power of the reference model is significant at ≈ 32% of the poloidal one up to $\ell < 20$ (Figure 5a), but below the median of the plate tectonic models (Figure 1) across all degrees (Figure 6), and the time-variable
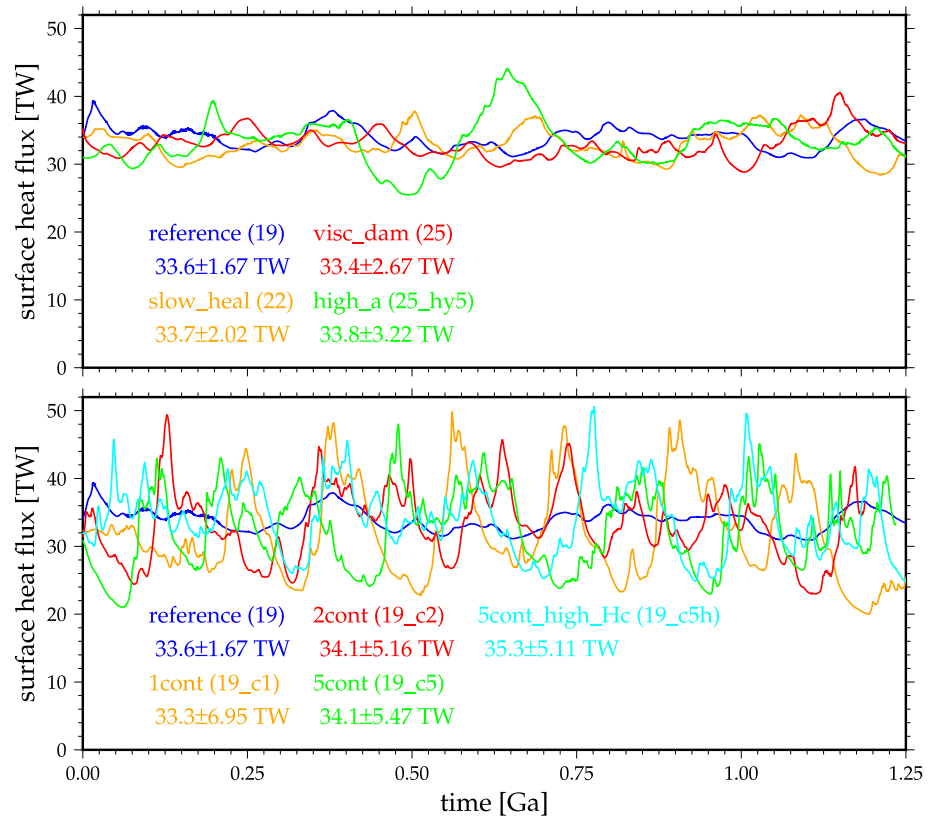
Figure 4. Comparison of bulk temporal convective behavior as exemplified by total surface heat flux for a representative model time period for all models discussed in the main text (Table 1) for oceanic lithosphere only (top) and once continents are included (bottom). Values provided underneath the legend state arithmetic mean and standard deviation.

ratio is 0.32 ± 0.07. One particular discrepancy is that of low toroidal power for $\ell = 1$, the NR component, which is very small for the oceanic lithosphere-only models. This finding is consistent with the expectation that fractionation-associated lateral viscosity variations such as due to strong continental keels may be needed (Becker, 2006; Zhong, 2001), and discussed for models with continental rafts below.
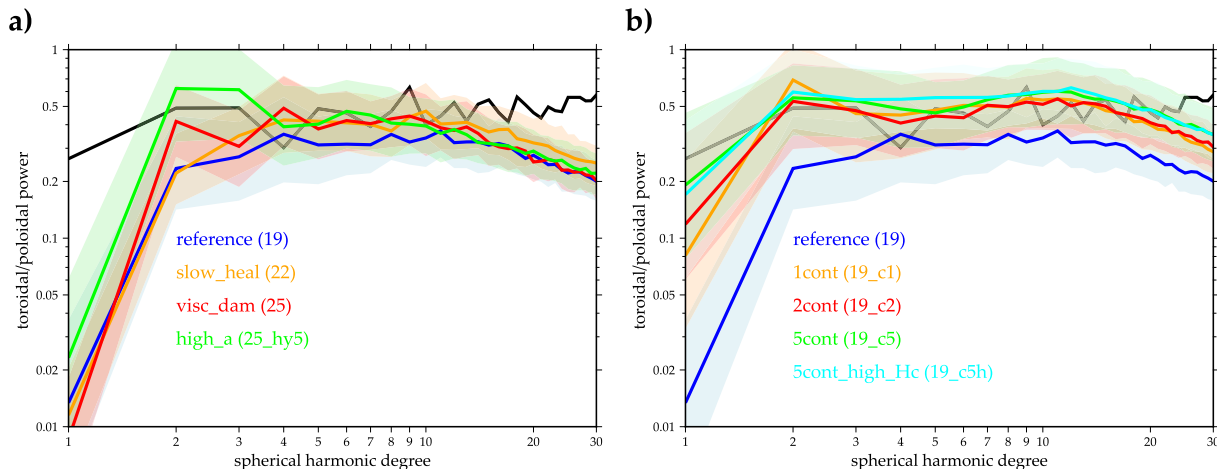

Figure 5. (a) Median toroidal to poloidal power (lightly shaded region indicating 25/75% range) for the different damage models of Table 1. Black line is the median value of the plate model of Müller et al. (2016) as per Figure 1e. (b) TPR for models with continents. See Figure 6 for complete poloidal and toroidal spectra and decay fits.
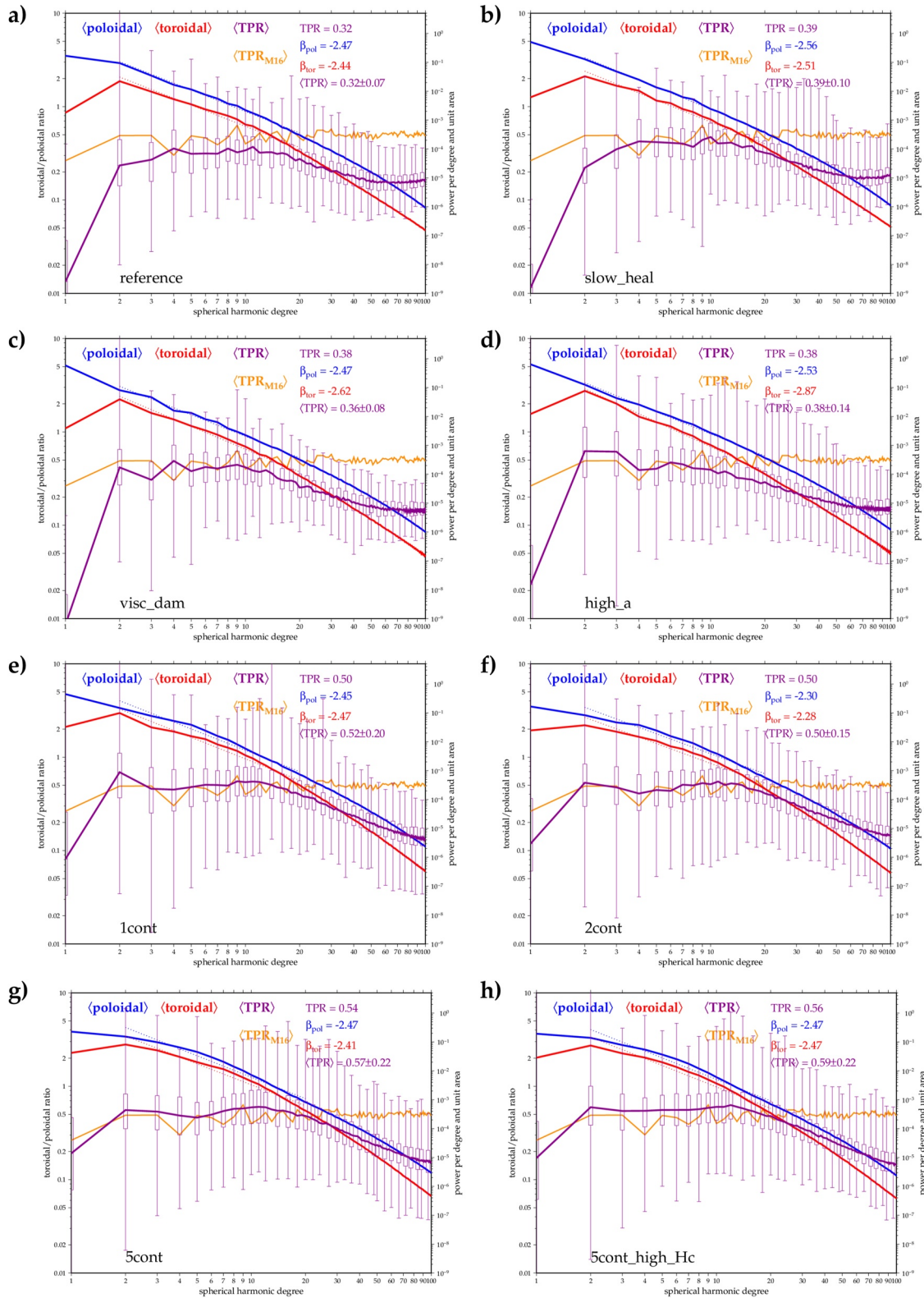
Figure 6. Surface velocity power spectra for all major models 19, 22, 25, 25_hy5, 19_c1, 19_c2, 19_c5, and 19_c5h ((a–h), Table 1). Blue, red, and magenta lines show the median power spectra for poloidal and toroidal motions, and their ratio (TPR), respectively, and box-whisker plots for the TPR indicate 25/75% quartiles and extreme values, respectively. Dashed lines from $2 \leq \ell \leq 20$ indicate power-law decay fits to the median spectra with ℓ^{β}, and best-fit β values stated in the legend as well as the mean TPR ratio across those degrees, and the temporal fluctuations, $\langle TPR \rangle$ as in Figure 1. $\langle TPR_{M16} \rangle$ is the TPR from the median power spectra of Müller et al. (2016) back to 140 Ma, as in Figure 1e.

The median poloidal and toroidal power spectra decay roughly with a power-law between $\ell = 1$ and $\ell \lesssim 20$ at decay exponents of $\beta \approx -2.5$ and -2.4, respectively (Figure 6). This is a slightly less steep decay than what is seen for the plate motions of Figure 1 which show $\beta \approx -2.8$. This indicates that the equivalent plateness is close to what is inferred from plate motions for the Cenozoic, but there is more intraplate deformation in the models than what is represented in the deforming plate models of Figures 1c and 1f.

The geodetic and geological models show a more rapid decrease of poloidal power, and hence an increase in TPR at $\ell \gtrsim 50$, whereas the convection models see a TPR trend reversal at $\ell \gtrsim 30$, on top of a decrease after roughly constant TPR from $2 \lesssim \ell \lesssim 12$. This corresponds to spatial scales D of $\sim$700 and $\sim$400 km for convection models and geodetic models, respectively. For $\ell \gtrsim 40$, the geodynamic model TPR stabilizes at $\sim$0.2. Resolution tests indicate that this asymptote is shifted to $\sim$0.25 for the higher resolution comparisons we explored which implies a loss of resolution. We, therefore, focus our discussion on a comparison of the TPR for degrees $\lesssim$20.

3.1.2. Mantle Heterogeneity Spectra

Another approach to assess which features of convection models might be related to present-day mantle convection is by comparison of the mantle structure power spectra (Figures 2b and 2c). Those depth-dependent spectra reflect the aforementioned mix of plate sizes, as shown in the surface velocity fields, with some large plates organizing the flow. When we compare the typical range of depth-dependent power as indicated by the spectral moment, we can see that the depth dependence is broadly similar to that inferred from seismic tomography (Figure 2a).

The spectrum with the highest ℓ spectral moment is found within and below our mechanical asthenosphere, at $\gtrsim$300 km depth where the confluence of radial viscosity variations, internal heating, and the "melt" viscosity reduction lead to lower viscosities in our models (Figure A1; cf. Foley & Becker, 2009). We expect tomography to image a similar asthenosphere, but the spectral moment of maximum higher ℓ power would lead us to infer a boundary layer that is shallower by $\sim$100 km. This is the case even though tomography includes the compositional effects of continental lithosphere, absent in these convection models. Along with the aforementioned plate speed underprediction, this is another indication that our models are still not quite at the convective vigor of Earth, in particular when viewed through the thermal boundary layer thickness (Figure A1).

When comparing tomographic and convective spectra, there is a lack of sub-lithospheric structure for $\ell \gtrsim 20$ in Figures 2b and 2c compared to Figure 2a, presumably because those shorter wavelength structures are not reliably globally imaged by current seismic tomography (e.g., Ritsema et al., 2007). We also see a secondary increase in ℓ of the convection spectral moment at $\sim$1,000 km (Figure 2b) due to the deep, slab reorganization consequences of time-variable plate motions, even in the absence of phase transitions or additional lower mantle viscosity increases. This suggests a note of caution when interpreting seismic tomographic signals for the present-day mantle. Given that our models do not include lower mantle chemical anomalies and are purely internally heated, we see a monotonous decrease of the typical ℓ from the spectral moment below $\sim$1,500 km.

Figures 2b and 2c show a scaled version of the spectral moment from tomography, multiplying the curve of Figure 2a by $\ell^{1.4}$ to roughly match the results from the convection models. This modification can be viewed as a visual aid, or a simple correction of the tomographic filtering that results from regularized inversions with incomplete data coverage. A similar enhancement of higher ℓ power would roughly correct for the tomographic loss of toroidal power from circulation modeling documented for the mid-mantle by Bull et al. (2010), for example,

While we know that the degree of bottom heating and other contributions can modify the spectral content with depth (e.g., Bunge et al., 1997; Deschamps & Tackley, 2009; Foley & Becker, 2009), comparison of the tomographic and model-produced character of convection with depth in Figure 2 appears thus quite favorable compared with the low Rayleigh number, visco-plastic results by Foley and Becker (2009). This indicates that the addition of an asthenosphere and higher convective vigor does indeed improve the match to observations.

In terms of dominant structure in the convection models as a function of spherical harmonic degree over all depths, we can see that the overall character of temperature structure is dominated by $1 \leq \ell \leq 3$ power (Figures 2b and 2c). The time-dependent nature of convection means that the mantle temperature state fluctuates between patterns akin to the $\ell = 1$ and $\ell = 2$ dominated structure as in Figures 2b and 2c (cf. Zhong et al., 2007), with much time spent in intermediate states. When we depth-average the maximum power degree below the surface
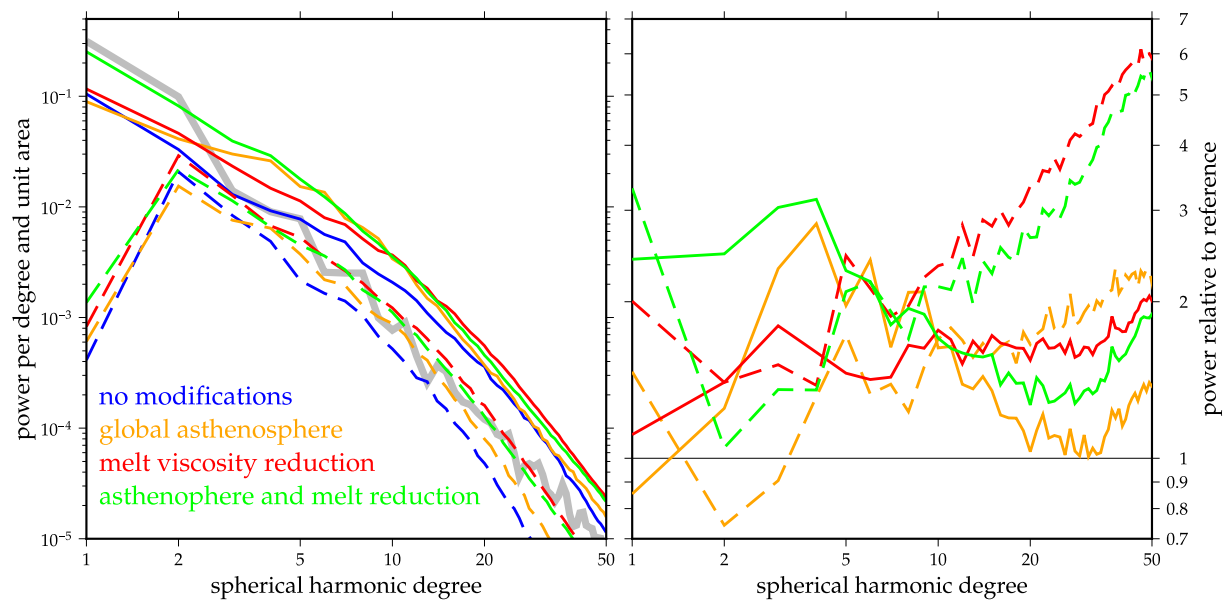
Figure 7. Comparison of the time-averaged median poloidal (solid) and toroidal (dashed) power per spherical harmonic degree, ℓ, and unit area for a reference model without asthenosphere and melt viscosity reduction (Section 2.3) for a slightly reduced temperature-dependent reference model with $E = 30$ (left). Figure on the right shows the same power spectra but relative to the reference. Comparisons are for models where we add a global asthenosphere only, add a "melt" viscosity reduction only, and if both are included, as for our reference model in the main text. The gray line shows the power spectrum of a spherical harmonics expansion of a mask function which is unity within the Pacific and zero else (using MORVEL geometries, Section 2.1), and approximately follows the ℓ^{-3} decay of a pure step-function.

thermal boundary layer, the temporal median dominant degree for model 22 (Table 1) is ≈ 1.44 with standard deviation of 0.36.

3.1.3. Role of the Asthenosphere

Adding a global, reduced viscosity layer to a background mantle is expected to make surface motions in convection models more plate-like and longer wavelength (Bunge et al., 1997; Busse et al., 2006; Richards et al., 2001). When we compare our reference model which has such a viscosity reduction at asthenospheric depths (Section 2.3) to a model without a global asthenosphere, power spectra are indeed affected by a bump up in mid-wavelength poloidal flow (Figure 7).

The further addition of the "melt" viscosity formulation which lowers the viscosity underneath divergent plate boundaries enhances coherence near spreading centers, as expected (Tackley, 2000c), and leads to a strong increase in shorter wavelength toroidal power compared to models without such an addition (Figure 7). A caveat is that other choices of asthenospheric properties might have a larger effect on surface motions given our boundary layer thickness (Figure A1). However, in particular the $\ell \gtrsim 10$ degrees of toroidal power are found to be quite sensitive to the rheology of the asthenosphere underneath spreading centers (cf. Coltice et al., 2019; Tackley, 2000c).

3.2. Damage and Yielding

We now proceed to explore modifications of damage rheology based on the reference model of Figure 3. Figure 8 shows a snapshot of surface velocities for a model that enhances the effects of damage by means of modifying parameters such that there is a slower healing (model 22 of Table 1). The time dependence of heat transport is comparable to the reference model at $\approx 6\%$ temporal fluctuations in heat flux (Figure 4). Figure 5a shows that the toroidal:poloidal ratio (TPR) is enhanced across wavelengths for the increased memory model, however, up to on average $\approx 39\%$, with time-variations of 0.39 ± 0.1, and a steeper decay of the spectrum at $\beta \sim -2.6$ (Figure 6).

By comparison with Figure 3, we can see that the corresponding enhanced effects of damage tend to lead to a more complex evolution of spreading centers, for example, (Figure 8). The evolution of divergent plate boundaries is now showing more frequently features such as undulations of divergent plate boundaries, overlapping spreading centers, and microplates (Figure 9). Any such statements about morphology and planform of convection are
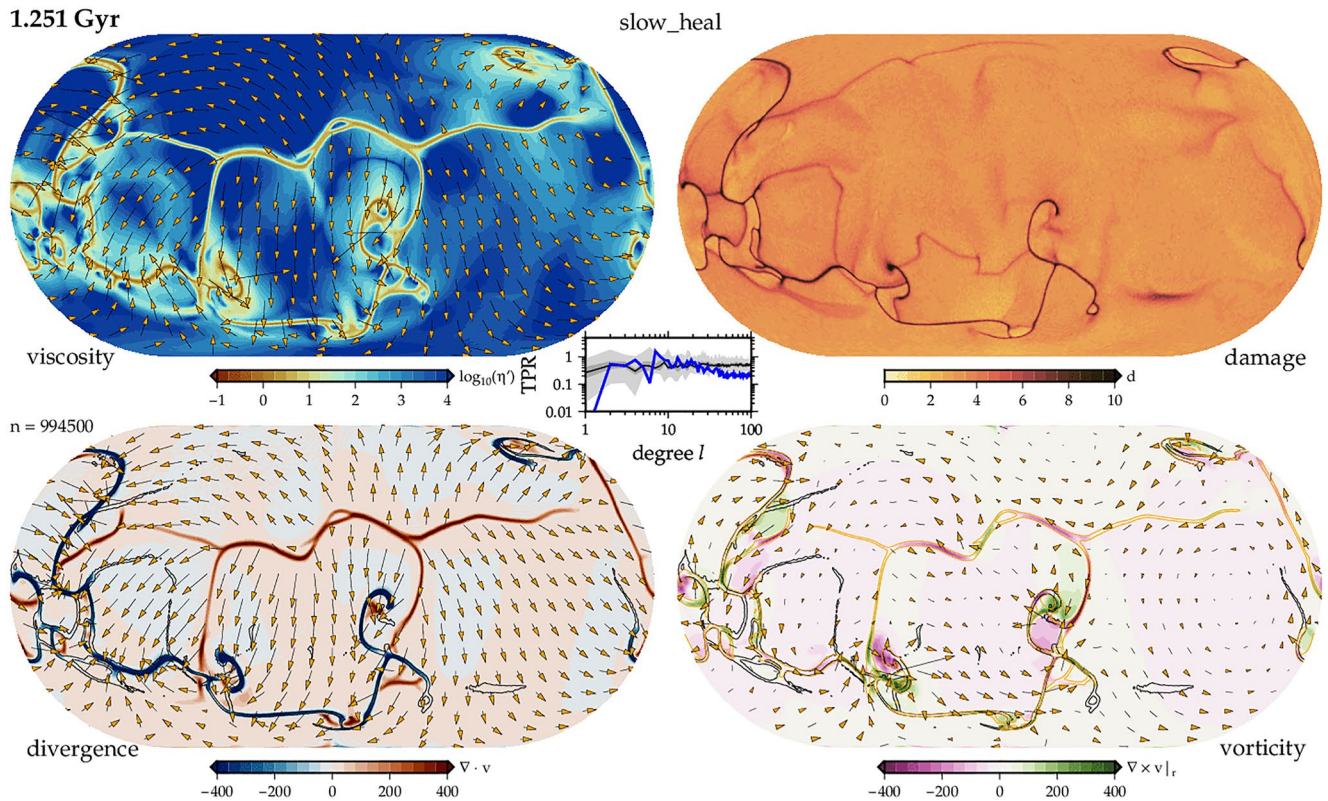
Figure 8. Surface kinematics of the slow-healing damage model (22 of Table 1), for details see Figure 3.

subject to large temporal fluctuations, as can be seen, for example, in the movies of the time evolution in Appendix A and the range of variations of the TPR spectra in Figure 5.

Figure 9 illustrates a typical regional tectonic evolution for this model. Note the undulated spreading center in the west and a tiny plate bound by all spreading triple junctions on the far east (Figure 9a), as driven by subduction in the south. Subduction evolves from opposite-polarity, double trenches to a highly curved single trench. Along the western triple junction of the spreading center, overlapping spreading centers (Figure 9b) separate and then form a clockwise rotating microplate with a ~20 Myr lifetime (Figures 9c and 9d, cf. Hieronymus, 2004; Zatman et al., 2001). Subsequently, the southern spreading center is abandoned (see black damage contours in Figure 9e), and a new undulation in the northern spreading center forms. While not quite a sharp spreading center-transform offset, there are thus indications for something akin to the segmentation documented in models with higher viscosity contrasts (Langemeyer et al., 2021), and higher regional resolution (Gerya, 2010). Many of such tectonic features are transiently contained in all of the models considered here, regardless of rheology, but we strive to comment on the more statistically robust, and typical, features of each model.

Surface dynamics are similar if the damage affects viscosity rather than yield stress (Figure A2; cf. Fuchs & Becker, 2021), albeit at slightly increased variability of heat transport with a standard deviation of ≈8% for the heat flux for model 25 of Table 1 (Figure 4). A comparison of power spectra indicates that the viscosity damage case does show a significant increase in $\ell = 2$ toroidal power, however, bringing the range from $\ell = 2\dots10$ within the values indicated by plate reconstructions (Figure 5a). Figure 10 shows the surface kinematics for a model where the background yield stress is additionally raised. In terms of power spectra, the response of moving closer to the stagnant lid regime is a steeper decay of toroidal power (Figure 6), which leads to the median TPR exceeding plate reconstruction values for low degrees (Figure 5a).

To explore the trade-offs between damage effects and background plasticity values, we also show results from a computation which has a slightly higher yield stress offset a, model 25_hy5 (Table 1). Considering the plate boundary evolution, this modification leads to more pronounced undulations of spreading centers, as in the snapshot of Figure 10, albeit at further increased episodicity of plate tectonic heat transport (≈10% temporal
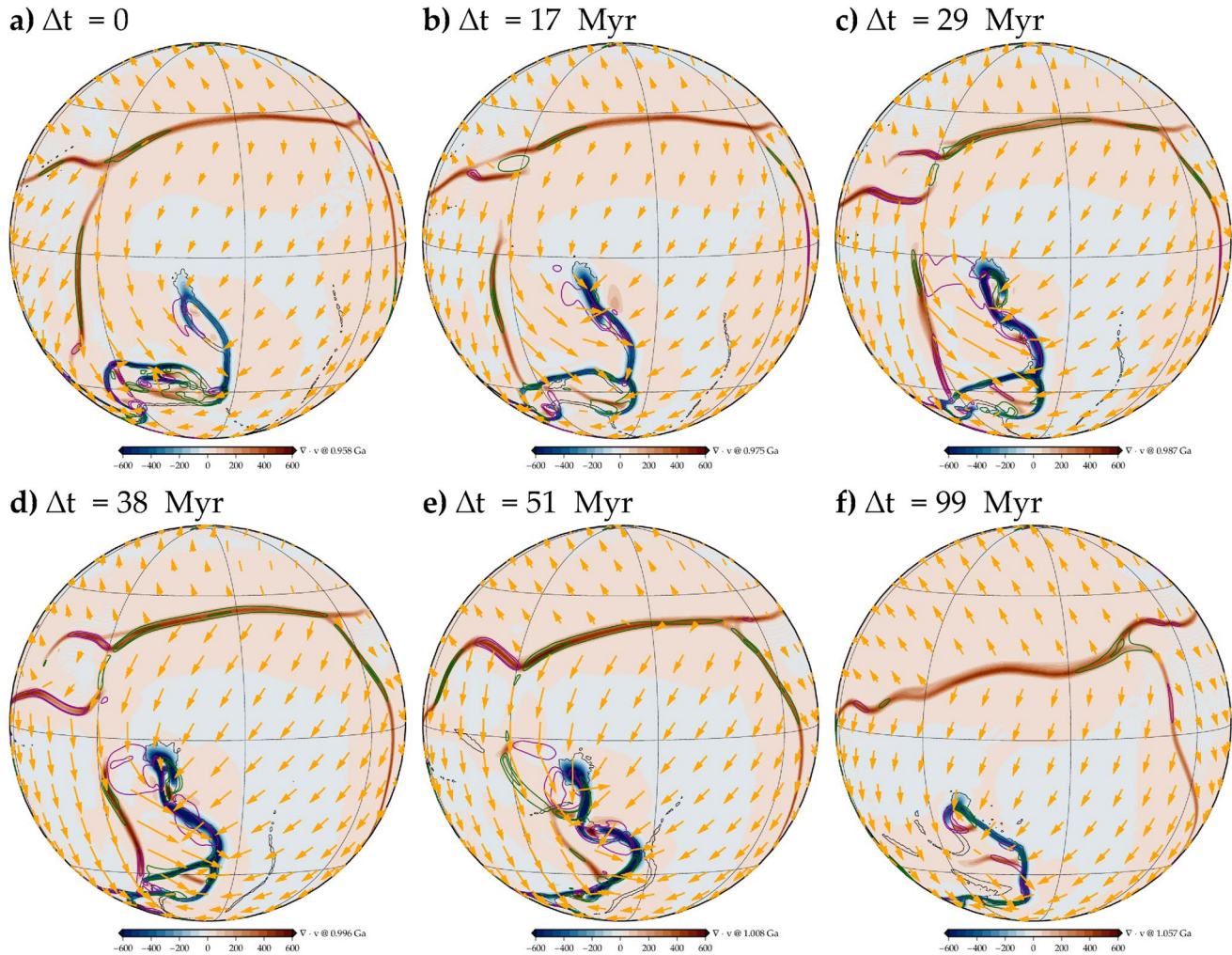
Figure 9. Evolution of a spreading center over time for the slow healing damage model (22 of Table 1, orthographic projection). Velocities shown with divergence in the background, as in Figure 8, and ±100 and ±200 vorticity contours in magenta and greed, respectively. Snapshots of the model evolution at the indicated times, with Δt being relative to panel (a); black damage contours are for $d = 5$.

variability, Figure 4). This substantiates that there is a subtle interplay between damage rheologies locally reducing viscosity or plastic yield stress due to strain-localization and accumulated damage (Fuchs & Becker, 2022), and the well-known general behavior that the planform of convection is quite sensitive to background visco-plastic yield stress (cf. Langemeyer et al., 2021; Mallard et al., 2016; Tackley, 2000b).

However, since we are also closer to a stagnant lid, with a possibly episodic intermediate regime (cf. Foley & Becker, 2009), the model shown in Figure 10 does also intermittently stagnate. This leads to overall more dramatic plate boundary reorganizations than any of the models at lower background yield stress. Even when avoiding near-episodic periods of convective transport, the model of Figure 10 shows the highest fluctuations of heat flux, ≈10%.

This model also shows the steepest power-spectral decay of the surface kinematics for the oceanic lithosphere-only models discussed here (Figures 6a–6d). Best-fit power-law exponents are $\beta \approx -2.5$ and -2.9 for poloidal and toroidal fields, respectively, comparable but still smaller than for the deforming plate reconstruction (Figure 1f). The high yield stress model has the largest fluctuations around the temporal mean TPR of 0.38 ± 0.14 (Figure 6d) which is similar to the Müller et al. (2016) inference of 0.43 ± 0.14 (Figure 1e). This suggests that more work is needed to establish the typical means and fluctuations from it for both geological constraints and geodynamic models.
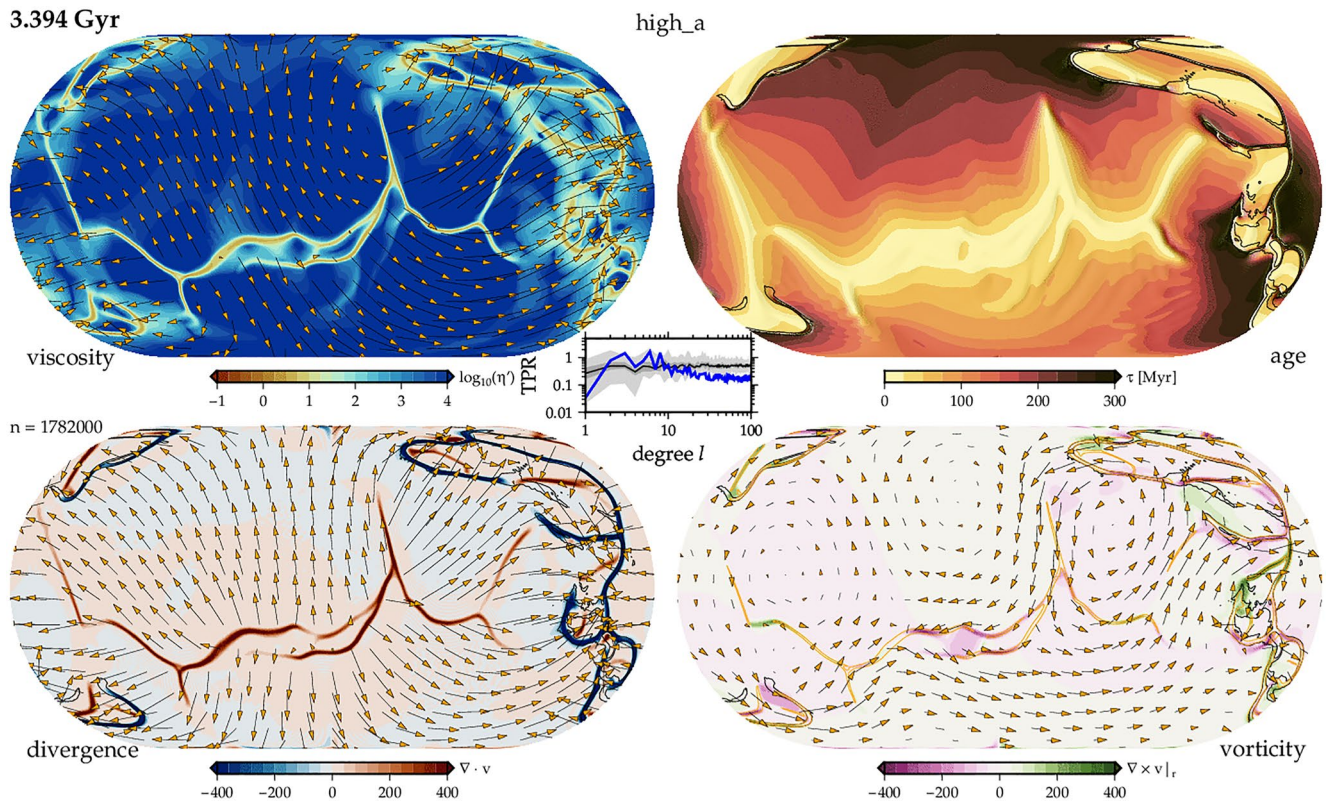
Figure 10. Surface dynamics of the high yield stress, η-damage model (25_hy5 of Table 1), for details see Figure 3, but top right shows effective seafloor age, τ, as computed from heat flux, q, from $q = 490 \left[\mathrm{mW/m^3}/\sqrt{\mathrm{Myr}} \right]/\sqrt{\tau}$, and limited to $q_{\min} = 20$ mW/m^3, instead of damage.

We have conducted a range of tests modifying the yield stress and damage formulations. Those models included having damage only reduce the yield stress, or viscosity, when material is under simple, rather than pure shear, deformation, inspired by the elastic damage models of Hieronymus (2004). Introducing such complexity modified the morphology of spreading centers, for example, by making overlapping segments as in Figure 9 more ubiquitous. However, we were not able to robustly, quantitatively distinguish between the effects of locally tuning plastic yield stresses and modifications of how damage applied given the computational demands of these global models.

3.3. Continents

What certainly has a strong effect on the overall planform of how convection is expressed at the surface including TPR is the inclusion of continental rafts (Figure 11). While the study of an idealized oceanic-only system is instructive, the additional complexity due to continents appears to be quite fundamental for plate-tectonic metrics.

Continents were implemented as high background yield stress, near neutrally buoyant (Ra$_b$/Ra = −0.75), circular regions of the lithosphere, making up ≈30% of the surface area (Section 2.3; Table 1). For our initial tests, these continental rafts were then subdivided into 1, 2, 3, and 5 initially separated, circular regions whose dispersal and assembly progress alongside the oceanic domain motions. Since continents show drastically reduced recycling rates compared to oceanic lithosphere, the effects of damage are expected to persist longer in the associated cold, thermo-chemical boundary layer.

Computations with continental rafts were initialized from a temperature snapshot of our continent-free reference model. We discuss the dynamics after some initial overturn times, and before models eventually ended up in an only episodically mobile state. This occurred for several of the continental models whereas the corresponding oceanic lithosphere only models remain mobile, likely because of the effectively globally modified plastic yield stress. Within our rheological choices and accepting the inference from Section 3.2, that is, that damage allows for
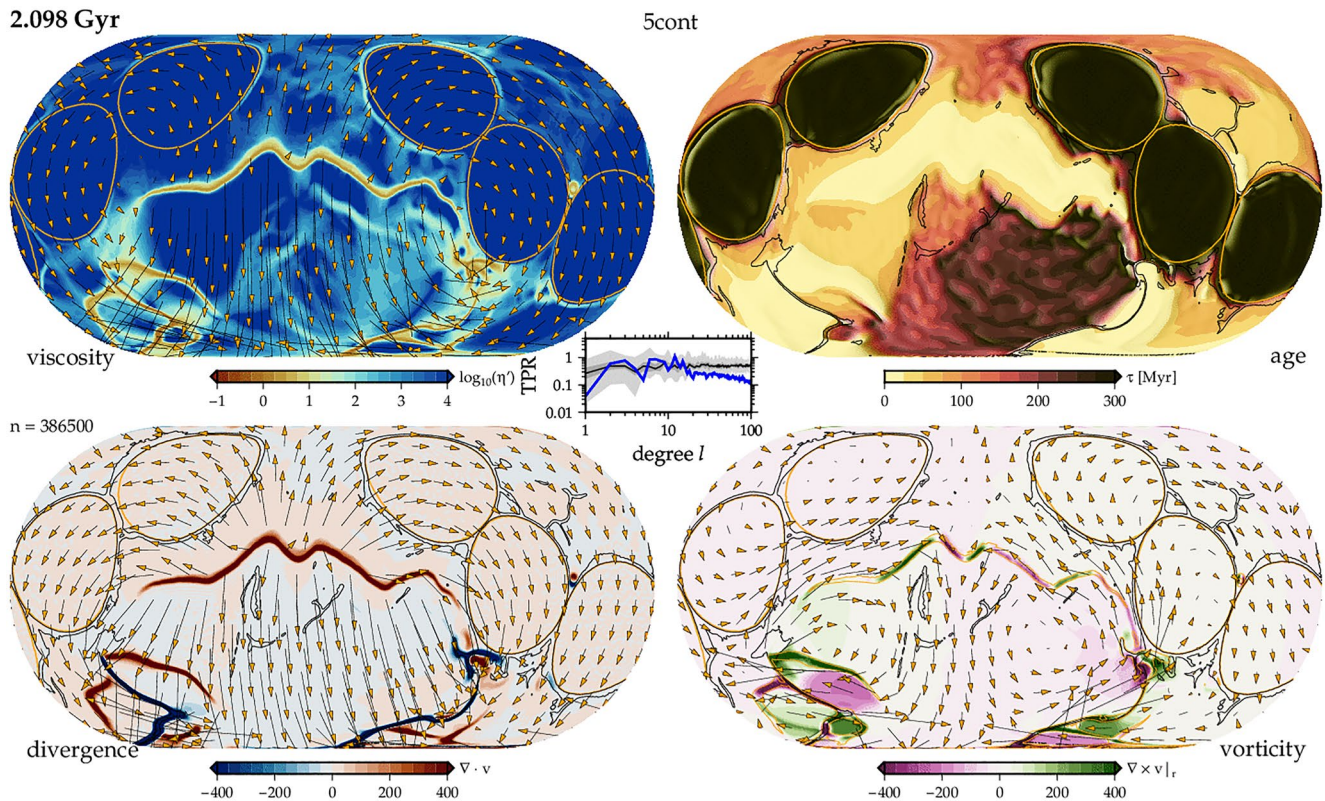
Figure 11. Surface dynamics of the five continental rafts model (19_c5 of Table 1), for figure details see Figure 3. Heavy orange lines are compositional $C = 0.5$ contours outlining the continental raft configuration; overall area $\approx 30\%$ for all continent models (see Figures 6 and 5b).

producing plate tectonic features within a mobile, rather than close to stagnant regime, this implies that the effects of continents may make damage even more important for sustaining mobile, plate-like convection.

Given the formulation of the damage rheology, continental rafts are able to store damage for longer times than oceanic regions, as on Earth. However, with our initial rheological choices, which are tailored toward maintaining stability, we do not find breakup of the original rafts for the reference parameters and circular, idealized raft geometry, and the total surface area of continents remains fairly stable, that is, little recycling.

Overall, the introduction of continental rafts has significant consequences on the time-variability of convection (Figures 4 and 6e–6h), substantiating the results of Rolf et al. (2012) and Coltice et al. (2012), for example, When considering heat flux variations, all continental models show significantly larger standard deviations (around similar mean heat flux) with typical values between ∼15% and 20% variations from the mean for the models considered (Figure 4). The role of continents for plate dynamics has been explored in visco-plastic computations (Rolf et al., 2018), but the kinematic power spectra and the role of damage remains under-explored.

Figure 5b shows the TPR for median power spectra for a range of continental models. When compared with the reference model, and the effect of different plate boundary rheologies (Figure 5a), it is clear that continental rafts also have a significant effect on toroidal motions. The mean TPR is elevated to ≈47% for a single continent, and ≈50%…56% for distributed continental rafts, while the high ℓ TPR is somewhat reduced because now a larger part of the surface is deforming in a relatively rigid fashion. Temporal fluctuations of the TPR are likewise elevated, where the continental models show a standard deviation of 0.15…0.22 (Figure 6).

One marked difference in the kinematic power spectra is that the introduction of even a single continent dramatically increases the $\ell = 1$ TPR, that is the NR component of the global surface velocities (Figure 5b). The more dispersed the continental area, the higher the NR component for our models considered. The five-continent model, shown as a snapshot in Figure 11, reaches NR values that are comparable to that inherent in the Müller et al. (2016) plate model. This continent-induced NR increase is expected given the role of continental versus
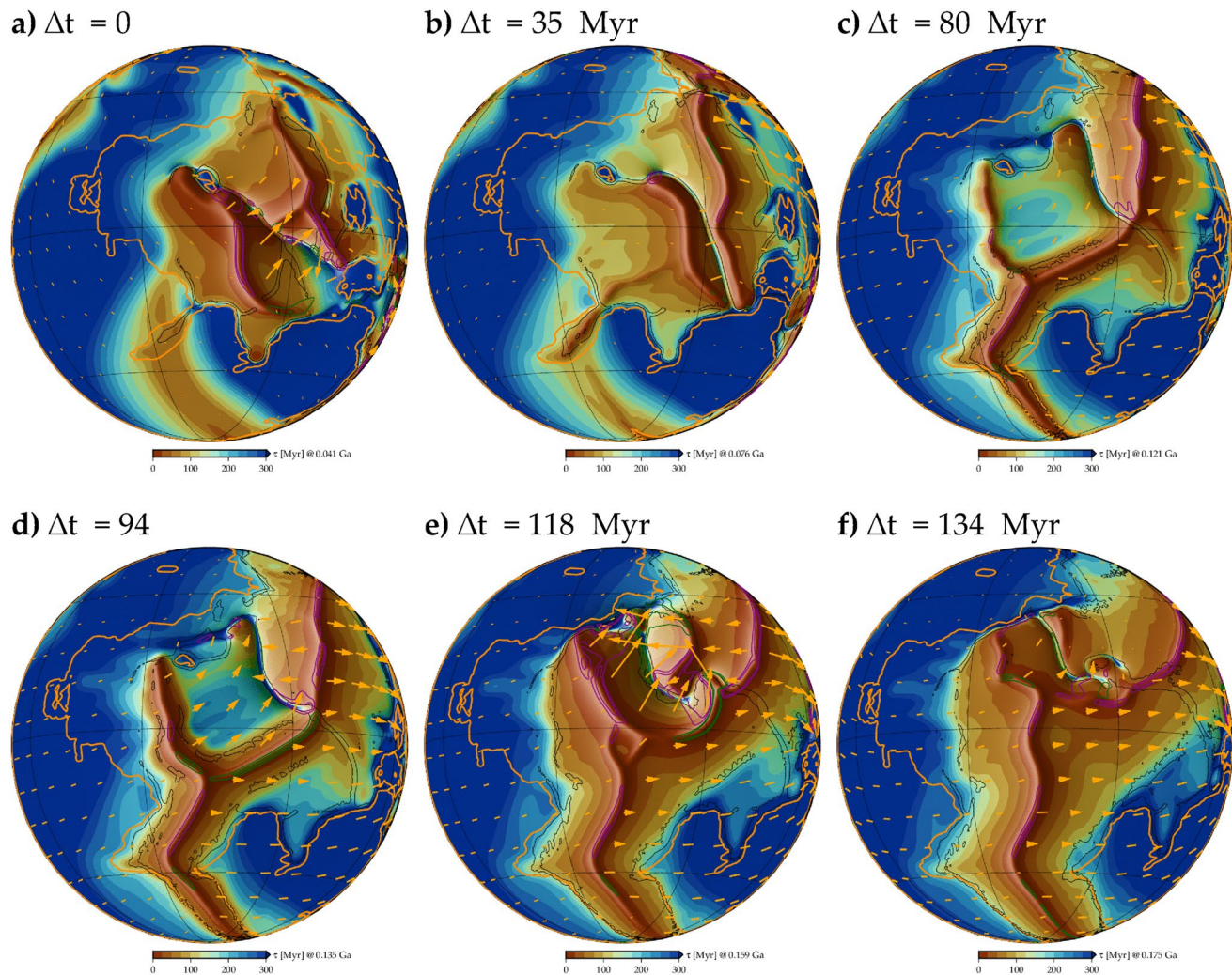
Figure 12. Breakup of a 250 Ma configuration supercontinent imposed based on the Matthews et al. (2016) plate reconstruction (orange outlines) arbitrarily placed over an upwelling upon initialization (see background heat flux, scaled to effective seafloor age as in Figure 10; shading is by the gradient of the poloidal potential). Six snapshots at the indicated times relative to panel (a); black contours show regions with $d = 5$ damage.

oceanic asthenospheric viscosity variations (Becker, 2006; Ricard et al., 1991; Rudolph & Zhong, 2014; Zhong, 2001), and the amplitudes are broadly consistent with those expected from 2-D cylindrical computations (Atkins & Coltice, 2021; Gérault et al., 2012).

When we consider the temperature distribution power spectra with depth, as in Section 3.1.2, we find that continental models that allow for dispersal of smaller rafts do spend more time in a mode which is dominated by $\ell = 2$ power with depth (cf. Zhong et al., 2007). Dispersal may be facilitated by the reduction of yield stress due to damage (cf. Rolf et al., 2018). While the signal is highly time-dependent (cf. Figures 2b and 2c), the higher internal heating concentration, five continent model (19_c5h of Table 1) has a temporal median, dominant mantle structure wavelength of $\ell \approx 2 \pm 0.23$ compared to the 1.44 ± 0.36 of continent-free model 22.

Figure 11 shows an example snapshot of a spreading center geometry whose shape is partially due to the reorganization of subduction zones around continents, implying some connection between intraoceanic features and continental configuration. Such a connection was discussed early on for ridge-transform offsets in nature given their counterparts in rifts after continental separation during the Wilson cycle. However, we know, for example, from the analog experiments by Oldenburg and Brune (1975) and Sibrant et al. (2021), that continents are not a required condition for ridge offsets. As in the analog experiments, we do see similar features for our oceanic lithosphere-only models (e.g., Figures 8 and 9), as was shown by Langemeyer et al. (2021).

While the role of continental viscosity and other properties in affecting overall plate speeds and the vigor of convection have been explored in visco-plastic modeling (Rolf et al., 2012, 2018), we varied a few of the parameters in our damage rheology models, including the modified heat flux boundary condition imposed by continental rafts. Figures 6 and 5b include power spectra from a five-continent model, for example, which has increased internal heating within continents, as would be expected from the concentration of incompatible elements after fractionation. The overall spectral character is similar to the model with the reference heat distribution, but toroidal power is increased further, to an average of ≈56%, which is slightly higher than the mean inferred from plate reconstructions (Figure 5b). These results emphasize that while features such as undulating spreading centers do not require the effects of continents, we cannot easily separate any of the kinematic quantities as inferred from plate reconstructions without accounting for the role of continents. Damage matters, but continents to an even larger extent.

Rolf et al. (2012, 2018) used a more easily deformable buffer zone around a stronger continental keel to allow for fragmentation of continental blocks, while avoiding the relatively fast recycling of continental material by subduction that ensues even if continents are made moderately high viscosity and neutrally buoyant (Lenardic et al., 2003; Yoshida, 2012). We might anticipate that our damage formulation may lead to the natural formation of such buffer zones in a dynamically consistent way.

This is the case, and damage can accumulate around the circumference of our continental rafts, and in some limited instances due to initialization and geometrical details, within the continents themselves. However, based on our initial tests, we were not able to find a suitably reduced continental yield strength for supercontinental breakup cycles to be sustained over many convective overturn times. Any initial breakup of the rafts as in Figure 11 is easy enough to achieve by reducing the continental yield stress. This leads to interesting, slab-driven continental rift formation and subsequent transition to an oceanic spreading center over ∼50…70 Myr. However, subsequently, continental fragments are dispersed in even smaller chunks, and the total surface area over ∼1 Gyr is reduced from the original 30% to ≲15% by recycling, depending on the yield stress reduction. How rapid is too rapid depends on the overall balance of recycling with fractionation and formation of continents, which is ignored here, and also somewhat uncertain for nature.

What our models certainly allow for is an exploration of scenarios of continental breakup which may be of interest for semi-dynamically consistent exploration of regional continental dynamics. Such scenario computations are akin to those explored by Coltice et al. (2019), for example, in terms of their general approach. Our models allow exploring the interplay between newly generated and existing sutures, due to damage memory (Fuchs & Becker, 2022), along with the dynamical evolution of the convective system. Figure 12 shows an example evolution of the regional tectonics in an alternative reality to the actual breakup of Pangea in terms of the separation of Africa and South America from Antarctica and India. We took the continental configuration from the plate reconstruction of Matthews et al. (2016) at 250 Ma and prescribed that geometry instead of generic circular rafts. The computation was then initialized from a mantle temperature snapshot during dynamic steady-date from our reference, oceanic lithosphere only computation. Parameters are as in the generic continental rafts explored above, but we apply a 50% reduced continental yield stress (continental a_c plasticity now five rather than 10 times that for oceanic plates, cf. Table 1) to allow for more ready dispersal of continental rafts.

The particular temperature snapshot used for initialization contained, by chance, a broad-scale upwelling in the geographic region of interest (Figure 12a) and could thus be considered as a rough proxy for a convection-driven supercontinental breakup scenario. Given the particular configuration of initial plate geometry and damage of Figure 12, we indeed see formation of a rift, breakup of the continental regions, and then formation of a new oceanic spreading center (Figures 12b and 12c, in the South). Subsequently, this model's evolution also maintains ≈36% continental surface area over ∼600 Myr, that is, very little continental recycling during the remainder of the model run.

While we did explore rafts of diamond shape rather than circular geometry to explore possible stress concentrations due to sharp edges, none of those diamond models showed clear raft separation as in Figure 12 without fast recycling. This indicates that the interplay between geometry and damage, as opposed to, or in addition to, the imposition of different continental lithospheric strength, may be a fruitful future avenue to pursue. We also use the Pangea scenario of Figure 12 to explore the robustness of tectonic features from higher-resolution computations (Figure A4); results in terms of supercontinental dispersal are quite similar, but the details of plate

boundary evolution and exact timing depend strongly on local tectonics, as exacerbated by slight differences in plate boundary strength.

4. Discussion

Few would question that the thermo-chemical component of convection at the root of the formation, recycling, and destruction of continental lithosphere is crucial for the overall evolution of our planet. However, it does indeed appear that even oceanic plate kinematics cannot be fully studied in isolation, perhaps to the chagrin of those seeking a physically simple description of Earth.

Both our oceanic lithosphere-only and continent-included computations with damage show undulated spreading centers, with features akin to ridge-transform offsets, albeit of transient nature (e.g., Figure 9). Yet, we do not see the relatively sharp, transform-like offset. along spreading centers which were documented by Langemeyer et al. (2021) based on their purely visco-plastic computations. Since we do not find any sharper fragmentation even for the higher-resolution computations we explored, we suggest that this difference might arise because our moderate small-scale viscosity variations, and the temperature-dependence of viscosity which is also somewhat smaller than that explored by Langemeyer et al., who also ran at higher convective vigor. Sorting out such differences further provides an important avenue to explore in future models, including in terms of the role of different temperature-dependent viscosity laws (Coltice, 2023; Stein & Hansen, 2013).

One general issue with global, visco-plastic mantle convection computations is that while they show some of the hallmarks of plate tectonics, plate convergence is often symmetrical in localized zones of downwellings, rather than showing one-sided, asymmetrical subduction (Foley & Becker, 2009; van Heck & Tackley, 2008). As in earlier work without damage (Foley & Becker, 2009), we do see transient one-sided subduction zone geometries due to slab rollback episodes, but more often, downwellings are symmetric. While divergent plate boundaries passively respond to the associated far-field slab pull forcing, we cannot rule out that more asymmetrical subduction may also affect spreading center morphology, and stabilize the behavior, perhaps along with more realistic rheologies which may require higher local resolution to properly resolve the dynamics.

Our undulated spreading center morphology is closer to the transients discussed by Coltice et al. (2019) for the evolution of oceanic basins after continental breakup. However, evolutionary scenarios with microplates (e.g., Figure 9) and the mix between small-scale and hemispheric plate boundaries (e.g., Figures 3 and 8) have not been widely discussed in dynamically consistent global computations. Transient geometries are also observed, for example, for regional models of ridge-transform fault offsets (Gerya, 2010; Püthe & Gerya, 2014), and it remains to be explored if different damage formulations (cf. Schierjott et al., 2020) alone may increase the lifespan sufficiently to declare victory in our efforts to explain tectonic features.

Is damage required for the features we see? We can find instances of highly transient, undulated spreading centers if the yield stress of purely visco-plastic rheology models is tuned to higher values. This highlights a major issue, trying to distinguish the effects of damage leading to locally reduced yield stress, as opposed to globally modified yield stress (cf. Fuchs & Becker, 2022). We are currently conducting regional computations to further explore these issues, but from our preliminary assessment, it appears that damage rheology is one way to produce Earth-like tectonic complexity such as in Figure 9 while remaining in a mobile rather than episodic state, at least for oceanic lithosphere-only models.

What is clear is that if pure visco-plastic rheologies are invoked to explain Earth's characteristic ridge-transform offset morphologies, then only very limited ranges of yield stress values appear permissible (cf. Langemeyer et al., 2021). If so, this likely indicates that there is a feedback mechanism underlying this only apparently plastic behavior, the nature of which remains to be determined. Even if the role of damage in the specifics of expressions of plate boundaries may be limited, we do of course know that rock rheology is not purely plastic and sutures play an important role for the evolution of plate tectonics, such as when previously failed rifts are reused during the Wilson cycle (e.g., Buiter & Torsvik, 2014; Gouiza & Naliboff, 2021; Huismans & Beaumont, 2003).

5. Conclusions

The addition of damage rheology to global, 3-D visco-plastic mantle convection computations produces Earth-like tectonic features in terms of a mix between large plates and complex, smaller-scale regional tectonics. Smoothly

undulated spreading centers evolve into overlapping ridges and microplates, at toroidal-poloidal power ratios similar to Earth. The variability of kinematics and heat transport are increased once continental rafts are included, indicating that any rheological formulation has to be explored in conjunction with the interactions between the oceanic plate—continental lithosphere system for a full understanding of planetary tectonics. Our models highlight potential avenues to conduct such analyses, from an ab initio perspective as well as when applied to specific continental rifting and regional plate boundary evolution scenarios.

Appendix A: Supplementary Information

This section provides additional results, including analysis from models not discussed in the main text.
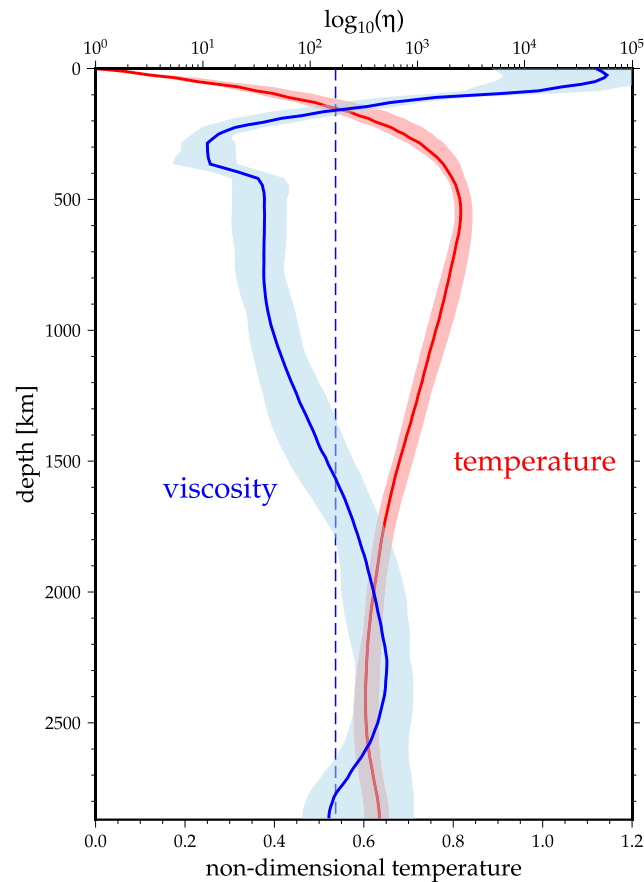

Figure A1. Horizontal temperature (red, non-dimensional) and viscosity (blue, non-dimensional on log scale) average against depth for the reference model (19 of Table 1), where solid lines are temporal median, and light-colored ranges indicate extreme ranges for the model times considered. The dashed vertical line is the volume-weighted, log average of viscosity.
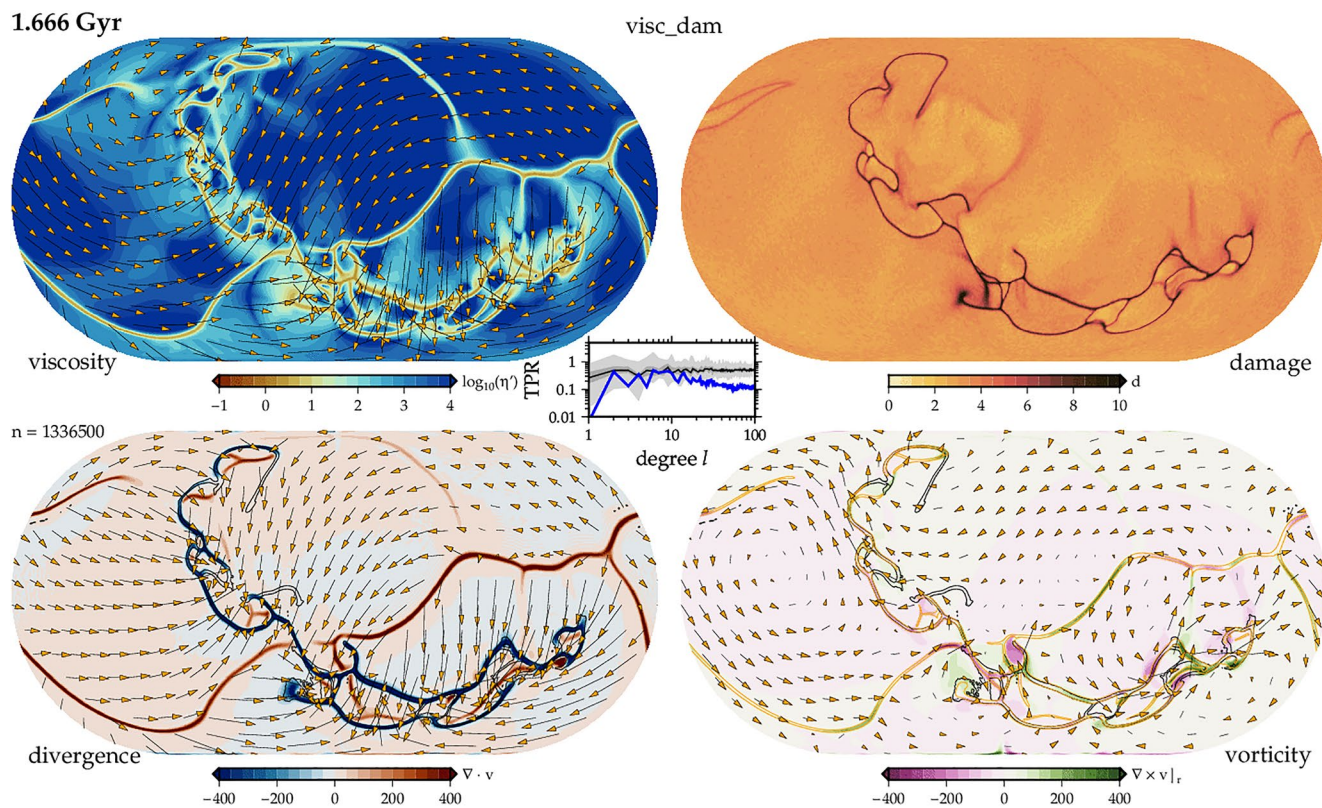
Figure A2. Surface dynamics of the slow healing, η damage model (25 of Table 1), for figure details see Figure 3.
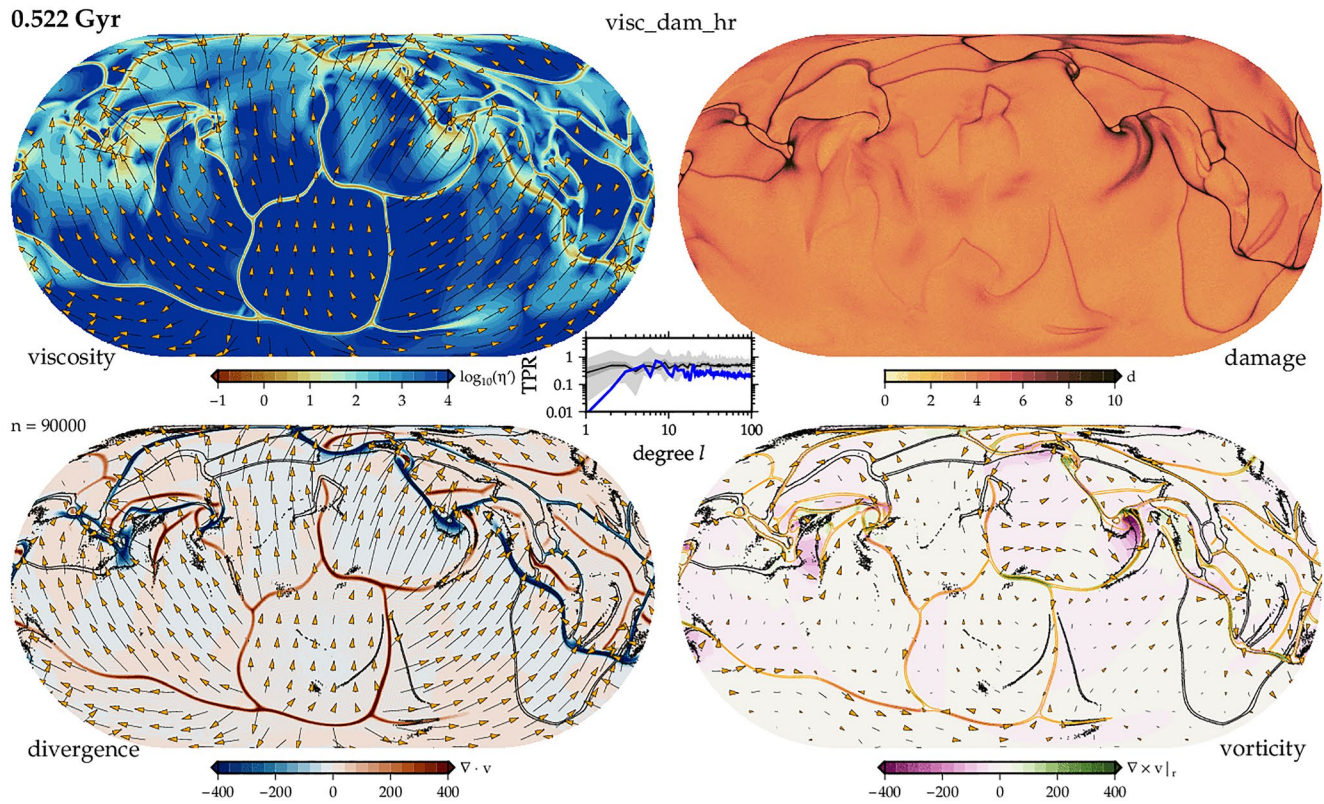
Figure A3. Surface dynamics of the slow healing, η damage model (25 of Table 1), as in Figure A2 (here, an earlier timestep is shown), but computed at a higher mesh resolution. For figure details see Figure 3.

1. Figure A1 shows the depth-dependent average non-dimensional temperature and viscosity of the reference model.
2. Figure A2 shows the surface kinematics for a snapshot for the slow healing damage model where d reduces viscosity rather than yield stress (model 25 of Table 1), plotted as in Figure 3. The main text shows the high background yield stress version of this model as Figure 10.
3. Figure A3 shows the surface kinematics for a snapshot for the slow healing damage model (model 25 of Table 1) as in Figure A2, but computed at higher resolution.
4. Figure A4 shows a breakup scenario starting as in Figure 12 but using a higher resolution computation.
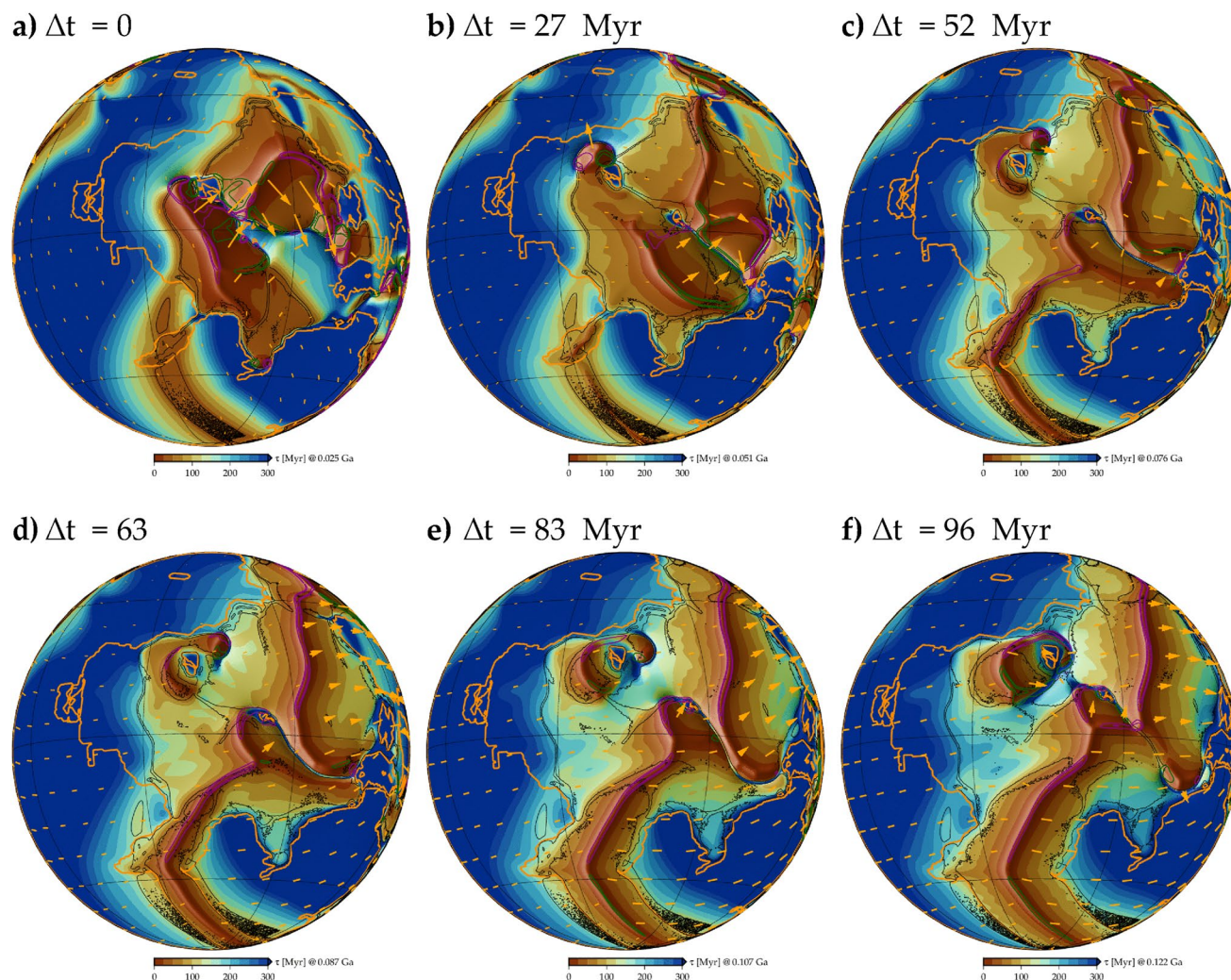
Figure A4. Breakup of a 250 Ma configuration supercontinent as in Figure 12, but using a higher resolution convection computation.

Data Availability Statement

We used the finite element software `CitcomS` and thank L. Moresi, S. Zhong, A. McNamara, and E. Tan for sharing their code developments, partly supported by the Computational Infrastructure for Geodynamics. Our extensions to `CitcomS` are available on github.com/geodynamics/citcoms under commit `2bda530`, and model input files and movies from our computations at Becker and Fuchs (2023).

References

Argus, D. F., Gordon, R. G., & DeMets, C. (2011). Geologically current motion of 56 plates relative to the no-net-rotation reference frame. *Geochemistry, Geophysics, Geosystems*, *12*(11), Q11001. https://doi.org/10.1029/2011GC003751

Atkins, S., & Coltice, N. (2021). Constraining the range and variation of lithospheric net rotation using geodynamic modeling. *Journal of Geophysical Research: Solid Earth*, *126*(10), e2021JB022057. https://doi.org/10.1029/2021jb022057

Becker, T. W. (2006). On the effect of temperature and strain-rate dependent viscosity on global mantle flow, net rotation, and plate-driving forces. *Geophysical Journal International*, *167*(2), 943–957. https://doi.org/10.1111/j.1365-246x.2006.03172.x

Becker, T. W., & Fuchs, L. (2023). Input files and movie visualizations for convection models discussed in Becker and Fuchs, "Generation of evolving plate boundaries and toroidal flow from visco-plastic damage-rheology mantle convection and continents", manuscript revised for G-Cubed [Dataset]. Zenodo. https://doi.org/10.5281/zenodo.10070094

Becker, T. W., Schaeffer, A. J., Lebedev, S., & Conrad, S. P. (2015). Toward a generalized plate motion reference frame. *Geophysical Research Letters*, *42*(9), 3188–3196. https://doi.org/10.1002/2015gl063695

Bercovici, D. (1995a). On the purpose of toroidal motion in a convecting mantle. *Geophysical Research Letters*, *22*(23), 3107–3110. https://doi.org/10.1029/95gl03082

Bercovici, D. (1995b). A source-sink model of the generation of plate-tectonics from non-Newtonian mantle flow. *Journal of Geophysical Research*, *100*(B2), 2013–2030. https://doi.org/10.1029/94jb02598

Bercovici, D., & Ricard, Y. (2013). Generation of plate tectonics with two-phase grain-damage and pinning: Source–sink model and toroidal flow. *Earth and Planetary Science Letters*, *365*, 275–288. https://doi.org/10.1016/j.epsl.2013.02.002

Bird, P. (2003). An updated digital model of plate boundaries. *Geochemistry, Geophysics, Geosystems*, *4*(3), 1027. https://doi.org/10.1029/2001GC000252

Boschi, L., & Becker, T. W. (2011). Vertical coherence in mantle heterogeneity from global seismic data. *Geophysical Research Letters*, *38*(20), L20306. https://doi.org/10.1029/2011GL049281

Buffett, B. A., Gable, C. W., & O'Connell, R. J. (1994). Linear stability of a layered fluid with mobile surface plates. *Journal of Geophysical Research*, *99*(B10), 1985–1990. https://doi.org/10.1029/94jb01556

Buiter, S. J., & Torsvik, T. H. (2014). A review of Wilson cycle plate margins: A role for mantle plumes in continental break-up along sutures? *Gondwana Research*, *26*(2), 627–653. https://doi.org/10.1016/j.gr.2014.02.007

Bull, A. L., McNamara, A. K., Becker, T. W., & Ritsema, J. (2010). Global scale models of the mantle flow field predicted by synthetic tomography models. *Physics of the Earth and Planetary Interiors*, *182*(3–4), 129–138. https://doi.org/10.1016/j.pepi.2010.03.004

Bunge, H.-P., Richards, M. A., & Baumgardner, J. R. (1997). A sensitivity study of 3-D spherical mantle convection at 10^8 Rayleigh number: Effects of depth dependent viscosity, heating mode and an endothermic phase change. *Journal of Geophysical Research*, *102*(B6), 11991–12007. https://doi.org/10.1029/96jb03806

Burke, K., Dewey, J. F., & Kidd, W. S. F. (1977). World distribution of sutures – The sites of former oceans. *Tectonophysics*, *40*(1–2), 69–99. https://doi.org/10.1016/0040-1951(77)90030-0

Busse, F. H., Richards, M. A., & Lenardic, A. (2006). A simple model of high Prandtl and high Rayleigh number convection bounded by thin low-viscosity layers. *Geophysical Journal International*, *164*(1), 160–167. https://doi.org/10.1111/j.1365-246x.2005.02836.x

Čadek, O., & Ricard, Y. (1992). Toroidal/poloidal energy partitioning and global lithospheric rotation during Cenozoic time. *Earth and Planetary Science Letters*, *109*(3–4), 621–632. https://doi.org/10.1016/0012-821x(92)90120-k

Coltice, N. (2023). Tectonics is a hologram. In J. C. Duarte (Ed.), *Dynamics of plate tectonics and mantle convection* (pp. 105–125). Elsevier.

Coltice, N., Husson, L., Faccenna, C., & Arnould, M. (2019). What drives tectonic plates? *Science Advances*, *5*(10), eaax4295. https://doi.org/10.1126/sciadv.aax4295

Coltice, N., Rolf, T., Tackley, P. J., & Labrosse, S. (2012). Dynamic causes of the relation between area and age of the ocean floor. *Science*, *336*(6079), 335–338. https://doi.org/10.1126/science.1219120

DeMets, C., Gordon, R. G., Argus, D. F., & Stein, S. (1990). Current plate motions. *Geophysical Journal International*, *101*(2), 425–478. https://doi.org/10.1111/j.1365-246x.1990.tb06579.x

Deschamps, F., & Tackley, P. J. (2009). Searching for models of thermo-chemical convection that explain probabilistic tomography II - Influence of physical and compositional parameters. *Physics of the Earth and Planetary Interiors*, *176*(1–2), 1–18. https://doi.org/10.1016/j.pepi.2009.03.012

Foley, B., & Becker, T. W. (2009). Generation of plate tectonics and mantle heterogeneity from a spherical, visco-plastic convection model. *Geochemistry, Geophysics, Geosystems*, *10*(8), Q08001. https://doi.org/10.1029/2009GC002378

Fuchs, L., & Becker, T. W. (2021). Deformation memory in the lithosphere: A comparison of damage-dependent weakening and grain-size sensitive rheologies. *Journal of Geophysical Research: Solid Earth*, *126*(1), e2020JB020335. https://doi.org/10.1029/2020JB020335

Fuchs, L., & Becker, T. W. (2022). On the role of rheological memory for convection-driven plate reorganizations. *Geophysical Research Letters*, *49*(18), e2022GL099574. https://doi.org/10.1029/2022gl099574

Gérault, M., Becker, T. W., Kaus, B. J. P., Faccenna, C., Moresi, L. N., & Husson, L. (2012). The role of slabs and oceanic plate geometry for the net rotation of the lithosphere, trench motions, and slab return flow. *Geochemistry, Geophysics, Geosystems*, *13*(4), Q04001. https://doi.org/10.1029/2011GC003934

Gerya, T. (2010). Dynamical instability produces transform faults at mid-ocean ridges. *Science*, *329*(5995), 1047–1050. https://doi.org/10.1126/science.1191349

Gouiza, M., & Naliboff, J. (2021). Rheological inheritance controls the formation of segmented rifted margins in cratonic lithosphere. *Nature comm*, *12*(1), 4653. https://doi.org/10.1038/s41467-021-24945-5

Hieronymus, C. F. (2004). Control on seafloor spreading geometries by stress- and strain-induced lithospheric weakening. *Earth and Planetary Science Letters*, *222*(1), 177–189. https://doi.org/10.1016/j.epsl.2004.02.022

Huismans, R. S., & Beaumont, C. (2003). Symmetric and asymmetric lithospheric extension: Relative effects of frictional-plastic and viscous strain softening. *Journal of Geophysical Research*, *108*(B10), 2496. https://doi.org/10.1029/2002JB002026

Jaupart, C., Labrosse, S., Lucazeau, F., & Marechal, J.-C. (2015). Temperatures, heat and energy in the mantle of the Earth. In G. Schubert (Ed.), *Treatise on geophysics* (2nd ed., pp. 223–270). Elsevier.

Jordan, T. H. (1978). Composition and development of the continental tectosphere. *Nature*, *274*(5671), 544–548. https://doi.org/10.1038/274544a0

Kreemer, C., Blewitt, G., & Klein, E. C. (2014). A geodetic plate motion and global strain rate model. *Geochemistry, Geophysics, Geosystems*, *15*(10), 3849–3889. https://doi.org/10.1002/2014GC005407

Landuyt, W., Bercovici, D., & Ricard, Y. (2008). Plate generation and two-phase damage theory in a model of mantle convection. *Geophysical Journal International*, *174*(3), 1065–1080. https://doi.org/10.1111/j.1365-246x.2008.03844.x

Langemeyer, S. M., Lowman, J. P., & Tackley, P. J. (2021). Global mantle convection models produce transform offsets along divergent plate boundaries. *Communications Earth & Environment*, *2*, 1–10. https://doi.org/10.1038/s43247-021-00139-1

Lavier, L. L., Buck, W. R., & Poliakov, A. N. B. (2000). Factors controlling normal fault offset in an ideal brittle layer. *Journal of Geophysical Research*, *105*(B10), 23431–23442. https://doi.org/10.1029/2000jb900108

Lenardic, A., Moresi, L. N., & Mühlhaus, H. (2003). Longevity and stability of cratonic lithosphere: Insights from numerical simulations of coupled mantle convection and continental tectonics. *Journal of Geophysical Research*, *108*(B6), 2303. https://doi.org/10.1029/2002JB001859

Lithgow-Bertelloni, C., Richards, M. A., Ricard, Y., O'Connell, R. J., & Engebretson, D. C. (1993). Toroidal-poloidal partitioning of plate motions since 120 Ma. *Geophysical Research Letters*, *20*(5), 375–378. https://doi.org/10.1029/93gl00168

Lu, C., Grand, S. P., Lai, H., & Garnero, E. J. (2019). Tx2019slab: A new p and s tomography model incorporating subducting slabs. *Journal of Geophysical Research: Solid Earth*, *124*(11), 11549–11567. https://doi.org/10.1029/2019jb017448

Mallard, C., Coltice, N., Seton, M., Müller, R. D., & Tackley, P. J. (2016). Subduction controls the distribution and fragmentation of Earth's tectonic plates. *Nature*, *535*(7610), 140–143. https://doi.org/10.1038/nature17992

Matthews, K., Maloney, K., Zahirovic, S., Williams, S. E., Seton, M., & Müller, R. (2016). Global plate boundary evolution and kinematics since the late Paleozoic. *Global and Planetary Change*, *146*, 226–250. https://doi.org/10.1016/j.gloplacha.2016.10.002

McNamara, A. K., & Zhong, S. (2004). Thermochemical structures within a spherical mantle: Superplumes or piles? *Journal of Geophysical Research*, *109*(B7), B07402. https://doi.org/10.1029/2003JB002847

Montési, L. G. J. (2013). Fabric development as the key for forming ductile shear zones and enabling plate tectonics. *Journal of Structural Geology*, *50*, 254–266. https://doi.org/10.1016/j.jsg.2012.12.011

Moresi, L. N., & Solomatov, V. (1998). Mantle convection with a brittle lithosphere: Thoughts on the global tectonic styles of the Earth and Venus. *Geophysical Journal International*, *133*(3), 669–682. https://doi.org/10.1046/j.1365-246x.1998.00521.x

Moresi, L. N., & Solomatov, V. S. (1995). Numerical investigations of 2D convection with extremely large viscosity variations. *Physics of Fluids*, *7*(9), 2154–2162. https://doi.org/10.1063/1.868465

Müller, R. D., Flament, N., Cannon, J., Tetley, M. G., Williams, S. E., Cao, X., et al. (2022). A tectonic-rules-based mantle reference frame since 1 billion years ago–implications for supercontinent cycles and plate–mantle system evolution. *Solid Earth*, *13*(7), 1127–1159. https://doi.org/10.5194/se-13-1127-2022

Müller, R. D., Seton, M., Zahirovic, S., Williams, S. E., Matthews, K. J., Wright, N. M., et al. (2016). Ocean basin evolution and global-scale plate reorganization events since Pangea breakup. *Annual Review of Earth and Planetary Sciences*, *44*(1), 107–138. https://doi.org/10.1146/annurev-earth-060115-012211

O'Connell, R. J., Gable, C. W., & Hager, B. H. (1991). Toroidal-poloidal partitioning of lithospheric plate motions. In R. Sabadini & K. Lambeck (Eds.), *Glacial isostasy, sea-level and mantle rheology* (pp. 535–551). Kluwer Academic Publishers.

Ogawa, M. (2003). Plate-like regime of a numerically modeled thermal convection in a fluid with temperature-pressure-and stress-history-dependent viscosity. *Journal of Geophysical Research*, *108*(B2), 2067. https://doi.org/10.1029/2000JB000069

Oldenburg, D. W., & Brune, J. N. (1975). An explanation for the orthogonality of ocean ridges and transform faults. *Journal of Geophysical Research*, *80*(17), 2575–2585. https://doi.org/10.1029/jb080i017p02575

Phillips, B. R., & Bunge, H.-P. (2005). Heterogeneity and time dependence in 3D spherical mantle convection models with continental drift. *Earth and Planetary Science Letters*, *233*(1–2), 121–135. https://doi.org/10.1016/j.epsl.2005.01.041

Püthe, C., & Gerya, T. (2014). Dependence of mid-ocean ridge morphology on spreading rate in numerical 3-D models. *Gondwana Research*, *25*(1), 270–283. https://doi.org/10.1016/j.gr.2013.04.005

Ricard, Y., Doglioni, C., & Sabadini, R. (1991). Differential rotation between lithosphere and mantle: A consequence of lateral mantle viscosity variations. *Journal of Geophysical Research*, *96*(B5), 8407–8415. https://doi.org/10.1029/91jb00204

Richards, M., Yang, W.-S., Baumgardner, J., & Bunge, H.-P. (2001). Role of a low-viscosity zone in stabilizing plate tectonics: Implications for comparative terrestrial planetology. *Geochemistry, Geophysics, Geosystems*, *2*(8), 1026. https://doi.org/10.1029/2000GC000115

Ritsema, J., McNamara, A. K., & Bull, A. L. (2007). Tomographic filtering of geodynamic models: Implications for model interpretation and large-scale mantle structure. *Journal of Geophysical Research*, *112*(B1), B01303. https://doi.org/10.1029/2006JB004566

Rolf, T., Capitanio, F. A., & Tackley, P. J. (2018). Constraints on mantle viscosity structure from continental drift histories in spherical mantle convection models. *Tectonophysics*, *746*, 339–351. https://doi.org/10.1016/j.tecto.2017.04.031

Rolf, T., Coltice, N., & Tackley, P. J. (2012). Linking continental drift, plate tectonics and the thermal state of the Earth's mantle. *Earth and Planetary Science Letters*, *351*, 134–146. https://doi.org/10.1016/j.epsl.2012.07.011

Rudolph, M. L., & Zhong, S. J. (2014). History and dynamics of net rotation of the mantle and lithosphere. *Geochemistry, Geophysics, Geosystems*, *15*(9), 3645–3657. https://doi.org/10.1002/2014gc005457

Schierjott, J. C., Thielmann, M., Rozel, A. B., Golabek, G. J., & Gerya, T. V. (2020). Can grain size reduction initiate transform faults? Insights from a 3-D numerical study. *Tectonics*, *39*(10), e2019TC005793. https://doi.org/10.1029/2019TC005793

Seton, M., Müller, R., Zahirovic, S., Gaina, C., Torsvik, T., Shephard, G., et al. (2012). Global continental and ocean basin reconstructions since 200 Ma. *Earth-Science Reviews*, *113*(3–4), 212–270. https://doi.org/10.1016/j.earscirev.2012.03.002

Sibrant, A. L. R., Davaille, A., & Mittlstaedt, E. (2021). Rheological control on the segmentation of the mid-ocean ridges: Laboratory experiments with extension initially perpendicular to the axis. *Earth and Planetary Science Letters*, *557*, 116706. https://doi.org/10.1016/j.epsl.2020.116706

Stein, C., & Hansen, U. (2013). Arrhenius rheology versus Frank-Kamenetskii rheology–Implications for mantle dynamics. *Geochemistry, Geophysics, Geosystems*, *14*(8), 2757–2770. https://doi.org/10.1002/ggge.20158

Tackley, P. J. (2000a). Mantle convection and plate tectonics: Toward an integrated physical and chemical theory. *Science*, *288*(5473), 2002–2007. https://doi.org/10.1126/science.288.5473.2002

Tackley, P. J. (2000b). Self-consistent generation of tectonic plates in time-dependent, three-dimensional mantle convection simulations 1. Pseudoplastic yielding. *Geochemistry, Geophysics, Geosystems*, *1*(8), 1021. https://doi.org/10.1029/2000GC000036

Tackley, P. J. (2000c). Self-consistent generation of tectonic plates in time-dependent, three-dimensional mantle convection simulations 2. Strain weakening and asthenosphere. *Geochemistry, Geophysics, Geosystems*, *1*(8), 1026. https://doi.org/10.1029/2000GC000043

Tackley, P. J., Stevenson, D. J., Glatzmaier, G. A., & Schubert, G. (1994). Effects of multiple phase transitions in a three-dimensional spherical model of convection in Earth's mantle. *Journal of Geophysical Research*, *99*(B8), 15877–15901. https://doi.org/10.1029/94jb00853

Tetley, M. G., Williams, S. E., Gurnis, M., Flament, N., & Müller, R. D. (2019). Constraining absolute plate motions since the Triassic. *Journal of Geophysical Research: Solid Earth*, *124*(7), 7231–7258. https://doi.org/10.1029/2019jb017442

Torsvik, T. H., Müller, R. D., van der Voo, R., Steinberger, B., & Gaina, C. (2008). Global plate motion frames: Toward a unified model. *Reviews of Geophysics*, *46*(3), RG3004. https://doi.org/10.1029/2007RG000227

van Heck, H. J., & Tackley, P. J. (2008). Planforms of self-consistently generated plate tectonics in 3-D spherical geometry. *Geophysical Research Letters*, *35*(19), L19312. https://doi.org/10.1029/2008GL035190

Wessel, P., Luis, J., Uieda, L., Scharroo, R., Wobbe, F., Smith, W. H., & Tian, D. (2019). The generic mapping tools version 6. *Geochemistry, Geophysics, Geosystems*, *20*(11), 5556–5564. https://doi.org/10.1029/2019gc008515

Yoshida, M. (2008). Mantle convection with longest-wavelength thermal heterogeneity in a 3-D spherical model: Degree one or two? *Geophysical Research Letters*, *35*(23), L23302. https://doi.org/10.1029/2008GL036059

Yoshida, M. (2012). Dynamic role of the rheological contrast between cratonic and oceanic lithospheres in the longevity of cratonic lithosphere: A three-dimensional numerical study. *Tectonophysics*, *532*, 156–166. https://doi.org/10.1016/j.tecto.2012.01.029

Zatman, S., Gordon, R. G., & Richards, M. A. (2001). Analytic models for the dynamics of diffuse oceanic plate boundaries. *Geophysical Journal International*, *145*(1), 145–156. https://doi.org/10.1111/j.1365-246x.2001.00357.x

Zhong, S. (2001). Role of ocean-continent contrast and continental keels on plate motion, net rotation of lithosphere, and the geoid. *Journal of Geophysical Research*, *106*(B1), 703–712. https://doi.org/10.1029/2000jb900364

Zhong, S., & Gurnis, M. (1993). Dynamic feedback between a continent like raft and thermal convection. *Journal of Geophysical Research*, *98*(B7), 12219–12232. https://doi.org/10.1029/93jb00193

Zhong, S., Zhang, N., Li, Z.-X., & Roberts, J. H. (2007). Supercontinent cycles, true polar wander, and very long wavelength mantle convection. *Earth and Planetary Science Letters*, *261*(3–4), 551–564. https://doi.org/10.1016/j.epsl.2007.07.049

Zhong, S., Zuber, M. T., Moresi, L. N., & Gurnis, M. (2000). Role of temperature-dependent viscosity and surface plates in spherical shell models of mantle convection. *Journal of Geophysical Research*, *105*(B5), 11063–11082. https://doi.org/10.1029/2000jb900003